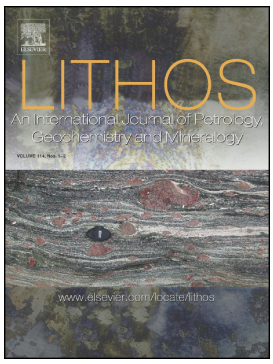

Geochemistry, petrogenesis, zircon U-Pb geochronology and Sr-Nd isotopic composition of Kuh-e-Shah volcanic rocks: Implications for an active continental margin along with eastern Iran during the Paleogene

Abbas Etemadia, Samaneh Nadermezerji, Mohammad Hassan Karimpour, Azadeh Malekzadeh Shafaroudi, José Francisco Santos, Sara Ribeiro

PII: S0024-4937(20)30415-1

DOI: https://doi.org/10.1016/j.lithos.2020.105778

Reference: LITHOS 105778

To appear in: *LITHOS*

Received date: 22 April 2020

Revised date: 11 September 2020

Accepted date: 11 September 2020

Please cite this article as: A. Etemadia, S. Nadermezerji, M.H. Karimpour, et al., Geochemistry, petrogenesis, zircon U-Pb geochronology and Sr-Nd isotopic composition of Kuh-e-Shah volcanic rocks: Implications for an active continental margin along with eastern Iran during the Paleogene, *LITHOS* (2020), https://doi.org/10.1016/j.lithos.2020.105778

Geochemistry, petrogenesis, zircon U-Pb geochronology and Sr-Nd isotopic composition of Kuh-e-Shah volcanic rocks: Implications for an active continental margin along with eastern Iran during the Paleogene

Abbas Etemadia* abbas.etemadi@mail.um.ac.ir, Samaneh Nadermezerji[a], Mohammad Hassan Karimpour[b], Azadeh Malekzadeh Shafaroudi[b], José Francisco Santos[c], Sara Ribeiro[c]

[a]Department of Geology, Faculty of Science, Ferdowsi University of Mashhad, Mashhad, Iran

[b]Department of Geology and Research Center for Ore Deposit of Eastern Iran, Faculty of Science, Ferdowsi University of Mashhad, Mashhad, Iran

[c]Department of Geosciences, Geobiotec Research unit, University of Aveiro, Aveiro, Portugal.

*Corresponding author.

Abstract

The Kuh-e-Shah complex includes the Paleogene volcano-plutonic belt of the Lut Block, eastern Iran. The volcanic rocks which outcropped in this complex mainly consist of trachy-andesites, andesites, and basaltic-andesites that mineralogically contain plagioclase, pyroxene, hornblende, and minor biotite and olivine. Geochemically, they have features typical of high-K calc-alkaline to shoshonitic magmas with enrichment in large ion lithophile elements (LILE), and depletion in high field strength elements (HFSE) and heavy rare earth elements (HREE). Chondrite-normalized REE plots show enrichment in light REE (4.9 < LaN/YbN < 11.6), Nb depletion and the slight negative Eu anomalies (Eu/Eu* = 0.80-0.99). Tectonic discrimination diagrams are used to infer a volcanic arc setting related to a continental subduction zone. It is concluded that the studied volcanic rocks have resulted from FC of a parental magma which formed by partial melting of the subducted oceanic crust and the overlying mantle wedge with spinel-lherzolite composition. Zircon U-Pb dating indicates an

age of 38.6 to 38.9 Ma for volcanic rocks (Late Eocene, Bartonian). Initial $^{87}Sr/^{86}Sr$ and $^{143}Nd/^{144}Nd$ ratios (0.704350-0.704820 and 0.512619-0.512779, resp.), are compatible with parental melts formation in a subduction mantle wedge. The εNdi values (+0.60 to +3.73) are in the range of mantle-derived melts. We suggest that volcanic rocks of the Lut Block are part of the Paleogene volcanism resulted from the Sistan oceanic crust subduction under the Lut Block during the Cretaceous.

Keywords: petrogenesis, REEs, zircon U-Pb geochronology, Sr-Nd geochemistry, Kuh-e-Shah, Lut Block.

1. Introduction

Iran is situated in the middle part of the Alpine–Himalayan orogenic belt that represents the Tethys Sea during the Paleozoic–Mesozoic transition (Ghorbani, 2013). According to the structural and geological divisions, Iran is divided into several structural units (Fig. 1a) and the eastern part of Central Iran is divided into two parts. A western part, known as the Lut Block (Stöcklin et al., 1965), and a strongly folded eastern part which has been named East Iranian Ranges (Berberian, 1977), Sistan Suture Zone (e.g., Tirrul et al., 1983; Walker et al., 2009) or Flysch zone (e.g. Ghorbani, 2013).

The Lut Block is surrounded by highly deformed domains of oceanic affinity and ophiolitic series along with flysch-type rocks especially at the eastern border with the Afghan Block (Fig. 1b; Stöcklin et al., 1972). It is believed that these rocks are remnants of a narrow arm of the subducted Neo-Tethys Ocean (Bagheri & Stampfli, 2008) in the east of Iran, i.e. the Sistan Ocean. The geological and metallogenic history of the Lut Block is marked by magmatic activities from the Jurassic to Quaternary (Karimpour et al., 2011). The volcano-plutonic rocks covered over half of the Lut block with up to 2000 m thickness, therefore the Tertiary period was of special importance, especially at the eastern part of the Lut Block

which also contains the Kuh-e-Shah volcano-plutonic complex. The investigated volcanic rocks covered the western part of this complex (Fig. 1b), between 58˚52′00″ to 59˚03′00″ latitude and 32˚21′00″ to 32˚27′00″ longitude.

In recent years, due to the importance of mineralization in eastern Iran, many studies have been conducted on intrusive rocks (more than volcanics) of the Lut Block and Kuh-e-Shah volcano-plutonic complex (e.g., Malekzadeh Shafaroudi et al., 2015; Samiee et al., 2016; Etemadi et al., 2018; Nadermezerji et al., 2018; Etemadi et al., 2019), regardless the importance role of volcanic rocks forming conditions during magma evolution. The origin of andesite is an important issue in petrology because andesite is the main eruptive product at convergent margins, corresponds to the average crustal composition, and is often associated with major Cu-Au mineralization (Chiaradia et al., 2011).

In this study, we present new geochemical (whole-rock major and trace element), isotopic (Rb-Sr and Sm-Nd), and geochronological (U-Pb) data from the Kuh-e-Shah volcanic rocks with a comparison to other scattered volcanic rocks throughout the Lut Block (Pang et al., 2013; Saadat & Stern, 2016; Javidi Moghaddam et al., 2019) to better understanding the Paleogene magmatism evolution of the Lut Block and to place constraints to the timing and onset of volcanism, its tectonic implications, the geochemical features of the mantle source involved in volcanic rocks genesis, petrogenetic processes and the controls of magma generation processes, the probable effects of fractional crystallization and crustal contamination, and geodynamic evolution of volcanic rocks which exposed in the western part of the Kuh-e-Shah volcano-plutonic complex.

2. Geological setting

According to Stöcklin (1968), the Lut Block is an irregularly micro-continental block outlined north-south-trending rigid mass, surrounded by the ranges of Central Iran (Tabas Block) in

the west and the Eastern Iran Flysch zone in the east by Nayband and Nehbandan faults, respectively. Large areas of the north-central, eastern, and western Lut Block are covered by volcanic rocks with peak activity during the Eocene in the north-central part. Based on scattered geochronology data, magmatism in this block is established by a variety of volcanic and volcaniclastic rocks, as well as subvolcanic stocks, started during the Middle Jurassic (Shah-Kuh (Esmaeily, 2001), Klateh Ahani (Moradi et al., 2011) and Surkh Kuh (Tarkian et al., 1983) granitoids;165-162 Ma), continued in the Late Cretaceous (Bajestan (Jung et al., 1983), Gazu (Tarkian et al., 1983) and Bazman (Berberian et al., 1982) granitoid; 76.6-74 Ma), Late Paleocene (Vaghi and Junchi (Jung et al., 1983) ignimbrites; 61-56 Ma), Middle Eocene to Early Oligocene (e.g., Malekzadeh Shafaroudi et al., 2015, Samiee et al., 2016, Etemadi et al., 2018, Nadermezerji et al., 2018, Etemadi et al., 2019; 39-30 Ma.) and finally ended with the eruption of Neogene basalts (Narrows (Jung et al., 1983); 42 Ma, Qal-e-Gonbad (Jung et al., 1983); 39.6 Ma, Mud (Jung et al., 1983); 31.4 Ma, and East Neh and Nayband (Walker et al., 2009); 15.5 to 1.74 Ma).

The andesitic volcanics erupted together with dacites and rhyodacites from Cretaceous (c. 65 Ma) to early Neogene (15.5 to 1.74 Ma). The Neogene and Quaternary volcanic rocks from the western and eastern margins of the Lut Block are similar in trace element chemistry to the average composition of oceanic island basalt and have a significant variation in chemistry with the Paleogene igneous rocks from the north-central part that follow both calc-alkaline and alkaline trends (Saadat & Stern, 2016). Most of the magmatic activity in the Lut Block occurred during the Middle Eocene to Early Oligocene (30-39 Ma: Karimpour et al., 2011). Mainly, the volcanic rocks are intruded by the next series of subvolcanic intrusions that cause various mineralizations (for more information see the introduction).

The eastern part of Iran had a complex tectonic history related to the evolution of Sistan Ocean, between Lut (in Iran) and Helmand (in Afghanistan) Blocks. This ocean probably was

opened by the Early Cretaceous (Babazadeh & De Wever, 2004) and its generation has been in progress during Middle Cretaceous (Zarrinkoub et al., 2012). The mechanism and final closure time of the Sistan Ocean (Late Cretaceous or Middle Eocene) remain poorly understood. Various models of evolution are wider presented at the geodynamic setting and tectono-magmatic model section.

The study area, located on the Sar-e-Chah-e-Shur and Mokhtaran 1:100000 geological sheets (Geological Survey of Iran, 1975; 1978), encompasses Paleocene-Eocene igneous rocks including a wide range of intrusives (mostly with intermediate composition; Figs. 2a, 2b, and 2c) along with the volcanic and volcaniclastic units exposed at low altitudes and plain (Fig. 2d, 2e, and 2f). Meanwhile, the volcanic units have the most expansion. According to our fieldwork and petrographic studies, the exposed rocks in the Kuh-e-Shah area can be divided into four units: 1) Paleocene to Middle Eocene sequence of folded volcano-sedimentary and volcaniclastic rocks; 2) Middle to Late Eocene sequence of intermediate volcanic and pyroclastic rocks (this study); 3) Late Eocene to Early Oligocene of mafic to intermediate subvolcanic rocks that intruded the volcanic units as stocks, and 4) Quaternary sediments including old and young terraces, recent alluvium, and gravel fans that cover most of the volcanic units.

The volcanic rocks have hill-shaped outcrops and their contact relationships with intrusive rocks well illustrate that they are older. The geological map of the study area is shown in Fig. 3, which is based on our field observations and relative age of component, petrographic studies, new age data from the region, and additional information from 1:100000 geological sheets.

3. Material and methods

More than 100 thin sections from the studied volcanic rocks were prepared and examined under the optical microscope (OLYMPUS CX31) both in the Economic Geology Laboratory of Ferdowsi University of Mashhad, Iran, and also at the Laboratório de Geologia Isotópica da Universidade de Aveiro, Portugal.

Fifteen fresh to very less altered samples were analyzed for whole-rock major elements by wavelength-dispersive X-ray Fluorescence (XRF) spectrometry using fused discs and by a Phillips PW 1480 XRF spectrometer at Amethyst Lab., Mashhad, Iran. For XRF, detection limits were reported as percentage (%) for major oxides and parts-per-million (ppm) for trace elements. Refractory and rare earth elements (REEs) were carried out using lithium fusion and Inductively Coupled Plasma Mass Spectrometry (ICP-MS) of powdered samples (0.2 g), following a $LiBO_2/Li_2B_4O_7$ fusion and nitric acid total digestion (LF 100), in the ACME Laboratories, Vancouver, Canada. This method offers increased sensitivity for 31 elements including REEs and trace elements occurring at low concentration levels (Cs, Ta, Th, U, Hf), with detection limits of around 0.01 ppm. In LF100-ICP-MS analysis, detection limits (DLs) change for REEs from 0.01 ppm (Tb, Tm, and Lu) to 0.3 ppm (Nd) and for other trace elements from 0.1 ppm (Rb, Zr, Nb, Y, Cs, Ta, Hf, and U) to 8 ppm (V). Whole-rock analytical results for major element oxides and trace elements are listed in Table 1.

Also, Two samples (trachy-andesite and andesite) were dated by LA-ICP-MS single zircon U-Pb analyses using a Tescan Cl detector instrument at the University of Idaho, Moscow, Idaho, Western United States. For this purpose, approximately 5 kg of rock was crushed to the grain size of <400 μm. More than 80 zircon grains (about 100) were isolated from samples using standard techniques includes using heavy liquid and magnetic separation, followed by hand picking under a binocular microscope. The selected crystals were placed on double-sided sticky tape and epoxy glue was then poured into a 2.5 cm diameter mound on top of the zircons, before cathodoluminescence (CL) imaging. CL imaging used to study the internal

structure of zircons after carbon coating, using a Tescan CL detector instrument. After CL imaging, the LA-ICP-MS U-Pb analyses were conducted using a New Wave Nd: YAG UV 213-nm laser coupled to a Thermo Finnigan Element 2 single collector, double-focusing, and magnetic sector ICP-MS at the GeoAnalytical Lab, University of Washington, WA, USA. Operating procedures and parameters are similar to those of Chang et al.'s (2006). U-Pb ages were calculated using Isoplot (Ludwig, 2007) in two different ways. The U-Pb isotope compositions and age data are listed in Table 2.

Based on petrographic and geochemical results, eleven samples were selected for Rb-Sr and Sm-Nd isotope analyses at the Laboratório de Geologia Isotópica da Universidade de Aveiro, Portugal, by chemical separation and mass spectrometry. In this method, the powdered samples were dissolved in two three-day steps with HF/HNO_3 and HCl (6.2 N) solution in Teflon PFA screw cap vial (Savilex) at 200 °C temperature, respectively. The Sr and Nd were separated from the dried sample using conventional ion chromatography technique in two stages; (a) separation of Sr and REE elements in an ion-exchange column with AG8 50W Bio-Rad cation exchange resin and (b) purification of Nd from other lanthanide elements in columns with Ln (ElChrom Technologies) cation exchange resin. Then, the Sr and Nd samples were loaded on a single Ta flament with H_3PO_4 and a Ta outer side flament with HCl in a triple flament arrangement, respectively. $^{87}Sr/^{86}Sr$ and $^{143}Nd/^{144}Nd$ isotopic ratios were determined using a multi-collector thermal ionization mass spectrometer (TIMS) VG Sector 54. The Nd and Sr natural isotopic ratios were normalized for mass fractionation relative to $^{88}Sr/^{86}Sr = 0.1194$ and $^{146}Nd/^{144}Nd = 0.7219$. The SRM-987 standard gave an average value of $^{87}Sr/^{86}Sr = 0.710268 \pm 13$ (N = 15; conf. lim = 95%, 2σ) and $^{143}Nd/^{144}Nd = 0.5120985 \pm 53$ (N = 11; conf. lim = 95%, 2σ) to JNdi-1 standard during this study. Rb-Sr and Sm-Nd isotope compositions are listed in Table 3, respectively.

4. Field observations and petrography

In the Kuh-e-Shah volcano-plutonic complex, in addition to intrusive and subvolcanic rocks that covered the middle heights of the study area with an east-west outcrop (Nadermezerji et al., 2018; Etemadi et al., 2019), five main volcanic and volcaniclastic units have been identified based on field observation, microscopic studies and geochemical discrimination: 1) trachy-andesites, 2) andesites, 3) basaltic-andesites, 4) dacitic to rhyodacitic tuffs, and 5) magmatic breccia (Fig. 3). Unlike the intrusions, the volcanic rocks are hill-shape in outcrops and cover the northern, western, and southern parts of the heights. Among them, trachy-andesites and andesites have the widest outcrops from the north to the south. The volcanic units are a little distinguishable in hand samples by their color and texture, so that, basaltic-andesite is more black color with amygdaloidal texture, andesite is gray with porphyry texture and trachy-andesite have a dark red color with few and small phenocryst. But their outcrops are hard to separate because of the covering by young terraces and high-level fans. Other volcanic rocks usually have small, scattered outcrops at the southeastern to the north and northwestern part of the Kuh-e-Shah complex (Fig. 3).

They generally have porphyritic textures (Fig. 4a). Other textures, such as sieve texture, glomeroporphyritic, trachytic, hiatal, and poikilitic are also present. Phenocrysts commonly make up 30 to 40 vol.% of the rock volume and include plagioclase (Some with zoning; Fig. 4b), amphibole (hornblende), clinopyroxene (augite) and biotite. Opaque minerals are mainly pyrite and minor magnetite. In some units, hornblende (rarely biotite) content exceeds 10 vol.% (Fig. 4c). The common presence of hornblende or biotite phenocrysts in the cited units indicates the high water content of the melts (Richards et al., 2012). Also, the existence of reaction rims around plagioclase and pyroxenes phenocrysts (Fig. 4d) and opasitization of hornblende to dark minerals (Fig. 4e) are observed in petrographic studies of the volcanic rocks thin sections. The existence of reaction rims around plagioclase and pyroxene

phenocrysts (Fig. 4d), zoning in some plagioclases (Fig. 4b and 4f), sieve texture and embayment of plagioclase phenocrysts are evidence for disequilibrium conditions during magma crystallization.

4.1. Trachy-andesites

Trachy-andesites together with some group of andesites (as an altered unit) have the widest outcrops in the north and west of the Kuh-e-Shah area (sample number: N-118, N-125, N-89, N-33, 15-E, 21-E, 26-E and N-111; Fig. 3). This unit consists of biotite-hornblende and hornblende bearing trachy-andesites (Figs. 3 and 4f). The trachytic texture is well visible in hand specimen. The rocks display porphyritic texture and phenocrysts include 35-40 vol.% plagioclase (0.2-1 mm), 10-12 vol.% pyroxene with euhedral-subhedral shape (~0.5 mm), 10-12 vol.% sanidine (0.1-0.2 mm), and about 3 vol.% biotite (0.2-0.5 mm). Various degrees of carbonatization and propylitic alteration can be distinguished in some samples. In these samples, plagioclase is partly altered into carbonate and argillic minerals and pyroxene are partly altered to chlorite.

4.2. Andesites

These volcanic units have outcrops at the southern part of the Kuh-e-Shah highlands. Some of those are not distinguishable from the trachy- andesite types due to alteration, so considered as altered andesite/trachy-andesite unit (samples number: 28-E, 41-E, 81-E and 83-E; Fig. 3). Based on their texture (mostly porphyry) and mineralogy, they can be divided into three different types covering biotite-hornblende bearing andesites (Fig. 4g), pyroxene-hornblende bearing andesites, and hornblende bearing andesites (Fig. 4c and 4e). Phenocrysts form 35-40 vol.% of the rocks and consist of plagioclase, hornblende, and pyroxene along with small amounts of biotite. Plagioclase is the main constituent (oligoclase) with 20-25 vol.%

abundance and 0.2 to 2 mm in diameter. Hornblende and pyroxene with ~10 vol.% (0.1 to 1 mm) and ~5 vol.% (0.2 to 0.5 mm) are other components and play the main role in rock classification. In the hornblende bearing andesite, hornblende content reaches up to 10 vol.% (Fig. 4c and 4e). Hornblende has green to brownish green color, euhedral shape and is mainly altered to Fe-oxides and opaque minerals (Fig. 4c). Biotite content is generally low (less than 4 vol.%) but in some units, its quantity increases up to 5 vol.%. In some samples, carbonatization and chloritic alteration are predominant: plagioclase is moderately altered into carbonate and argillic minerals, and pyroxene is altered into chlorite. The mafic minerals content is less than 1 vol.% and there are no veinlets in the rocks. Normal zoning in plagioclase is related to the mixing and digestion processes (McBirney, 2007) but the opasitization of hornblende signify unstable conditions during crystallization and may be due to the rapid uplift of the melt (Blatt et al., 2006).

4.3. Basaltic-andesites

The basaltic-andesite units encompass outcrops from the north to the west and southwest of the Kuh-e-Shah volcano-plutonic complex (samples number: N-92, N-162, and N-136; Fig. 3). Mineralogically, these rocks are composed of 20 vol.% plagioclase (0.7-3 mm), 13-15 vol.% pyroxene (0.5-2 mm, Fig. 4h) and minor olivine phenocrysts (3-4 vol.%, ~0.2-0.5 mm), approximately. They are dark and display porphyritic to amygdaloidal textures with fine-grained groundmass. Groundmass includes plagioclase and pyroxene along with minor glass. In this unit, plagioclase crystals have a composition close to andesine (An_{30}-An_{50}) and labradorite (An_{50}-An_{70}), based on their extinction angles. It is observed in some samples that during hydrothermal alteration, the plagioclase crystals are replaced by carbonate and minor sericite. Also, some of the olivines are partly altered to serpentine, Fe-oxide, and partially replaced by chlorite and opaque mineral assemblages (Fig. 4i).

4.4. Dacitic to rhyodacitic tuffs

Dacitic to rhyodacitic tuffs are exposed in the center and northeastern parts of the Kuh-e-Shah area, and usually have low topography together with conglomerates, magmatic breccias, and other volcano-sedimentary units. The dacites and tuffs of this unit are very fine-grained and relatively hard in hand specimen. The rock texture is pyroclastic including angled components of quartz (5-6 vol.%), plagioclase up to 0.4 mm (4-6 vol.%), K-feldspar up to 0.3 mm (1-2 vol.%), biotite up to 0.4 mm (~1 vol.%), and hornblende (~0.5 vol.%) in a fine-grained matrix. The space between the crystalline components is mainly filled with iron oxide and minor secondary carbonate minerals.

4.5. Magmatic breccia

This unit is exposed in the form of small, scattered outcrops at the southeastern to the southern part of the Kuh-e-Shah area, therefore, according to the scale of the geological map (Fig. 3), cannot be displayed. The magmatic breccia includes fragments of highly altered intrusive (with porphyry texture) and andesite rocks. Most fragments have rounded edges and their size varies from 3 to 50 cm and make up 45 to 50 vol.% of the rock. Most of the fragments consist of various types of porphyritic diorite, e.g., biotite diorite porphyry with 35-40 vol.% phenocrysts, hornblende diorite porphyry with 40-45 vol.% phenocrysts and other types of porphyritic intrusions such as monzonites. The matrix consists of a mixture of uncomminuted altered igneous rock (non-detectable) in fine-grained rock flour with high iron oxide content (the reason for the red color in hand specimen). Generally, rocks exhibit intense carbonate alteration.

5. Results

5.1. Whole-rock geochemistry

5.1.1. Major elements

Representative whole-rock major and trace element data of the Kuh-e-Shah volcanic rocks are given in Table 1. The volcanic rocks consist of trachy-andesite, andesite, and basaltic-andesite according to the Cox et al. (1979) classification diagram (Fig. 5a). The SiO_2 and MgO contents range between 53.08-62.70 wt.% and 0.76-5.81 wt.%, respectively (Table 1). K_2O + Na_2O content ranges from 4.91 to 7.35 wt.%. Trachy-andesites have higher K_2O + Na_2O content compared to the other volcanic rocks. Based on the AFM diagram (Irvine & Baragar, 1971; Fig. 5b), the volcanic rocks belong to the calc-alkaline series, whereas in the K_2O vs. SiO_2 diagram (Peccerillo & Taylor, 1976), they classify as high-K calc-alkaline to shoshonitic rocks (Fig. 5c). Most of the trachy-andesites and basaltic-andesites are located within the range of shoshonitic rocks whereas the andesites plot in the high-K calc-alkaline range.

When using SiO_2 as an index of differentiation abundances of the major elements vs. SiO_2 for the Kuh-e-Shah volcanic rocks (Fig. 6), SiO_2 content shows a negative correlation with TiO_2, Fe_2O_3, MnO, MgO, and CaO, and a positive correlation with Al_2O_3, Na_2O, K_2O, and P_2O_5, which suggests that fractional crystallization has been affected during magmatic evolution. Continental arc rocks generally have higher abundances of SiO_2, Al_2O_3, Na_2O, K_2O, and melt-mobile incompatible trace elements, but relatively lower abundances of MgO, Fe_2O_3T (Total Fe in Fe_2O_3), CaO, TiO_2, and melt-immobile compatible trace elements than oceanic arc rocks (Kelemen et al., 2014).

5.1.2. Trace and rare earth elements (REEs)

REEs are less affected by weathering and hydrothermal alterations than other elements. Therefore, their abundance pattern can be an indicator of the origin and other processes affecting the parent magma (Boynton, 1985). In the subduction zones, the major and trace

elements, and radiogenic isotope composition of magma is primarily dictated by subduction zone fluids that transfer elements from the subducting crust into the overlying mantle wedge. The subarc mantle is thus expected to be enriched in LILE (such as Cs, Rb, Ba, U, and Sr), LREE, Th, and Pb (water-soluble elements), unlike HSFE such as Nb, Ta, Ti, Zr and Hf and also HREE. Therefore, the mantle sources of magma appear relatively depleted in HFSE but enriched in Pb, resulting in negative Nb-Ta anomalies but a positive Pb anomaly (Zheng et al., 2019).

The chondrite-normalized rare earth element composition (Boynton, 1985) of the Kuh-e-Shah volcanic rocks are shown in Fig. 7a. REE patterns in these rocks show enrichment of light rare earth elements (LREE) relative to heavy rare earth elements (HREEs), similar to melts created in subduction zones. La_N/Yb_N and Ce_N/Yb_N ratios vary from 4.90 to 11.60 and 3.27 to 8.34 in the volcanic rocks, respectively. The Eu/Eu* ratio varies from 0.80 to 0.99, indicating a weak negative anomaly which may be variously explained by a low degree of plagioclase fractionation, high oxygen fugacity at the source, or insignificant contamination by continental crust (Tepper et al., 1993). High Sr/Y (23.1 to 100.5) and relatively high La/Yb (7.2 to 17.2) ratios with Eu/Eu* close to unity, indicates abundant early hornblende fractionation and suppression of plagioclase crystallization in a hydrous melt (Richards et al., 2012).

Due to their low mobility and low concentration in fluids and subducting sediments, the high field strength elements (HFSE) are not transported into the mantle wedge during subduction (Plank & Langmuir, 1998). Accordingly, their abundance can be used to assess the mantle wedge geochemistry prior to the start of the subduction process. As shown in the primitive mantle-normalized spider diagram (Sun & Mcdonough, 1989; Fig. 7b), there are significant negative anomalies of HFSE such as Nb, Ti, Zr, and Y compared with positive anomalies of large ion lithophile elements (LILE) such as Cs, K, Th, U, and Sr. These are

characteristics of magmas associated with subduction zones (e.g., Wilson, 1989; Gill, 2010) and magmas generated in an arc-related source (Kelemen et al., 2003).

The Kuh-e-Shah volcanic rocks have $(Nb/Zr)_N$ ratios between 0.44 and 0.74. In the $(Nb/Zr)_N$ versus Zr diagram (Thiéblemont & Tegyey, 1994), the samples with continental arc affinity plot within the subduction-related field (Fig. 8). The Dy/Dy* and Dy/Yb (representing the MREE/HREE ratio) ratios are potentially powerful tools to represent good information about the mantle sources and petrogenetic processes. Dy/Dy* is defined by interpolation between La and Yb (Davidson et al., 2013). The Dy/Dy* ratio for Kuh-e-Shah volcanic rocks change between 0.54 and 0.68 (i.e. less than 1) and Dy/Yb ranges from 1.49 to 1.98 (i.e. low ratio relative to MORB). The contrasting effects of different minerals in controlling REE patterns, such as garnet versus amphibole and clinopyroxene, are clear. Amphibole and clinopyroxene are the only major minerals capable of significantly decreasing Dy/Dy*, but amphibole has greater leverage, and correspondingly leads to decreasing Dy/Yb, whereas clinopyroxene has less effect on Dy/Yb. Nevertheless, it is still amphibole and clinopyroxene that control the capacity to significantly decrease Dy/Dy* (Davidson et al., 2013).

5.2. U-Pb zircon dating

U-Pb zircon dating was carried out at the GeoAnalytical Lab, University of Washington, Washington, United States. Cathodoluminescence (CL) images were obtained at the University of Idaho before the dating studies. CL images of zircons were acquired to characterize the internal features of zircons such as growth zones and inclusions to provide a base map, a powerful tool for placing the laser pits in the homogeneous parts of the crystals.

Zircons obtained from the selected volcanic samples (118N: trachy-andesite and 28E: andesite) are white to colorless and elliptical (Fig. 9). According to the size and internal textures under CL images, the zircon grains can be divided into three groups. Group 1 zircons

including the majority of grains, range in length from 50 to 100 μm and show variable oscillatory bands from the core to rim, suggesting changes in crystallization conditions. Group 2 zircons show typical magmatic textures with thick oscillatory bands ranging in length from 100 to 150 μm, and group 3 zircon grains are homogeneous without any zoning, showing gray-colored cores mantled by bright rims and displaying a typical core to rim texture.

More than 100 zircon grains obtained from each sample, meanwhile 69 zircons (35 zircons from trachy-andesite and 34 zircons from andesite) were selected for LA-ICP-MS U-Pb dating. From 35 zircon data of trachy-andesite, two data are deleted because of 2σ Abs Error more than 4 Ma (4.5 and 5.8 Ma). Except for one zircon with an age of 59.7 Ma (probably the inherited zircon), other ages change in a restricted range between 36.9 and 41.1 Ma, with the weighted mean ages of 38.9 ± 0.6 Ma for 32 zircon (errors shown are 2σ). For andesite, all of the 34 selected zircons analyzed that exposed ages from 36.7 to 40.4 Ma with the weighted mean ages of 38.6 ± 0.5 Ma (errors shown are 2σ) (Table 2). The average contents of ^{238}U and ^{232}Th are equal to 422 and 179 ppm in trachy-andesite zircons and 392 and 153 ppm in andesite zircons. Also, the average natural $^{207}Pb/^{235}U$ and $^{206}Pb/^{238}U$ ratios are similar in trachy-andesite and andesite zircons and change between 0.042 and 0.006. Weighted mean $^{206}Pb/^{238}U$ ages are denoted at the 95% confidence levels (2σ). Isotopic ages are presented in TuffZirc graphics (Figs. 10a and 10c) and Concordia diagrams (Figs. 10b and 10d).

5.3. Sr-Nd isotopic composition

In the continental subduction zone, fractional crystallization (FC) cannot change the radiogenic isotope compositions of residual melts, and assimilation fractional crystallization (AFC) processes can not explain the radiogenic isotopic features of most andesites. Regardless of the various factors, continental arc andesites are more enriched in radiogenic

isotopes (i.e. Sr, Nd, Hf, and Pb) and melt-mobile incompatible trace elements (Kelemen et al., 2014).

The Kuh-e-Shah volcanic rocks have high Sr (646.8 to 1809.9 ppm) and low Rb contents (35.9 to 101.6 ppm). Low Rb/Sr ratios (0.028-0.129) might indicate the preservation of an early stage of parent magma evolution because Sr tends to become concentrated in plagioclase during fractional crystallization and leaving Rb in the liquid phase, results an increase in the Rb/Sr ratio of the residual magma over time (Kendall et al., 1995). The Kuh-e-Shah volcanic rocks are not highly fractionated as suggested by SiO_2 contents < 62.7%. The $^{87}Sr/^{86}Sr$ and $^{143}Nd/^{144}Nd$ isotopic ratios of the Kuh-e-Shah volcanic rocks were determined on eleven whole-rock samples. The $^{87}Sr/^{86}Sr$ and $^{143}Nd/^{144}Nd$ initial isotope ratios vary between 0.704350-0.704820 and 0.512619-0.512779, respectively (recalculated to an age of 38.6 Ma; Table 3). εNd(i) values range from +0.60 to +3.73; thus the samples have relatively homogeneous Sr-Nd isotopic values. εNd(i) changes depending on the processes under which rocks are formed and also on the types of rocks that interacted with magma prior to eruption (Hong et al., 2004). The different chemical behavior of Sm and Nd during mantle melting results in low and negative εNd(i) values of the continental crust, whereas positive values for the Kuh-e-Shah volcanic rocks (+0.60 to +3.73) are commonly related to mantle-derived melts. In the εNd(i) versus $(^{87}Sr/^{86}Sr)i$ diagram (Fig. 11), all samples plot within the "mantle array" close to the Bulk Earth values.

6. Discussion

6.1. Petrogenesis

The SiO_2 contents of the Kuh-e-Shah volcanic rocks range from 53 to 62 wt %, while the SiO_2 contents of melts directly produced by partial melting of mantle material are less than 57 wt % (Baker et al., 1995), suggesting that these rocks do not represent the primary magma

derived from partial melting of the mantle. Similarly, the Mg# values of primitive arc melts are generally >70 (Schmidt & Jagoutz, 2017), compared with <45 of the studied rocks, meaning that these volcanic rocks were formed from mantle-derived magma after a fractional crystallization in magma chamber (Xu et al., 2019). This interpretation is supported by the lower contents of some compatible elements in the volcanic rocks. For example, the Cr (8–53 ppm) and Ni (5–18 ppm) contents of the samples are considerably lower than those of primitive arc magma (Cr = 364 ppm, Ni = 168 ppm) (Gudnason et al., 2012). Al_2O_3 in orogenic volcanic rocks varies from 16 to 18 wt.% (Gill, 1981), while this parameter varies between 14.29-16.14 wt.% in the Kuh-e-Shah volcanic rocks.

Our samples defined the significant correlation of SiO_2 with other major oxides and trace elements (Figs. 6 and 13), reflective of significant fractional crystallization during magma evolution. The Kuh-e-Shah volcanic rocks show high MgO contents relative to those of experimental crustal melt, suggesting that the volcanic magmas cannot have originated from partial melting of crustal materials. Experimental studies on melting have shown that continental crust melts are usually sodium-rich (Rutter et al., 1998), but our samples are high-K calc-alkaline to shoshonitic. Therefore, the Kuh-e-Shah volcanic rocks were not derived from a predominant crustal source.

The incompatible trace element distribution patterns of the Kuh-e-Shah volcanic rocks show similarity with typical arc andesites (from the Andes; e.g., Feeley & Davidson, 1994) and bulk continental crust (Rudnick & Fountain, 1995). The striking similarity of continental crust to arc andesites is partly been due to the incorporation of the crust by evolving magmas during differentiation to andesite. Nevertheless, the broad similarities in characteristics such as relative enrichments in LILE (Cs, Ba, Rb, K) and depletion in Nb appear to be fundamental features of the mantle source (Davidson et al., 2005).

6.2. Magma source

It is generally believed that fluids derived from subducted oceanic crust and the mantle wedge are depleted in HFSE because these elements are highly stable in refractory mineral phases (e.g., Ionov & Hofmann, 1995; Ayers, 1998). So, the high LILE/HFSE and LREE/HREE ratios may indicate that the melts originated from the subducted crust and overlying mantle wedge. Nb depletion is a typical feature of slab dehydration and melting processes in subduction zones, and its increase reveals mixing with continental crust (Wilson, 1989). Zr/Y ratio can be used to distinguish between oceanic and continental volcanic arc settings (Pearce, 1983) with ratios >3 representing continental volcanic arc settings (Fig. 12a). The Zr/Y ratio of the Kuh-e-Shah volcanic rocks vary between 2.97 and 7.05. In the Rb/Zr versus Nb (Brown et al. 1984; Fig. 12b) diagram, the Kuh-e-Shah volcanic rocks are located in the field of continental margin arc/primitive island arc with low maturity. The Th_N versus Nb_N diagram (Saccani, 2014; Fig. 12c) shows a tectonic affiliation to an active continental margin volcanic arc related to convergent plate setting for the Kuh-e-Shah volcanic rocks.

The high La/Nb and Ba/Nb ratios of the Lut Block volcanic rocks are consistent with the characteristics of arc volcanic rocks (Figure 13a; Li et al., 2013), which are generally considered to be related to subduction. Given that the Sm/Yb ratio depends on the mineralogical composition of the source region, the Sm/Yb versus La/Sm ratio can be used to estimate source composition (Shaw, 1970). Accordingly, the Kuh-e-Shah volcanic rocks might have been originated from partial melting of an enriched mantle with the spinel-lherzolite composition (Fig. 13b; Shaw, 1970). The Nb and Zr contents of volcanic rocks are higher than those of N-MORB, implying their generation from a non-depleted mantle source or through low degrees of partial melting (Sun & McDonough, 1989). The small presence (or absence) of garnet in the source conforms with low $(La/Yb)_N$ and $(Ce/Yb)_N$ ratios.

The garnet-free mantle has a modest influence over the REE elements, only La being significantly more incompatible during melting; thus melts from low pressure melting in the mantle have low values of Dy/Yb while La/Yb shows some variation. By contrast, garnet-bearing mantle lithologies retain Yb in preference to either Dy or La, and the compositions of melts produced in the presence of garnet extend to higher values of Dy/Yb (≈ >1.5). This shows that the La/Yb ratio is sensitive to the degree of melting whereas the Dy/Yb ratio is sensitive to the presence or absence of garnet (Sigurdsson et al., 2015). According to our sample REE patterns and what was said about the Dy/Dy* and Dy/Yb ratios in the REE section, although amphibole can play a greater role, we can conclude that clinopyroxene controls the capacity to relatively clear decrease in Dy/Dy* and Dy/Yb ratios.

Low $(Ce/Yb)_N$ ratio also confirms that the Kuh-e-Shah volcanic rocks derived from the upper mantle (Cotten et al., 1995). Slab-derived fluids or subducted sediments can enrich mantle sources, giving rise to enrichment in LILEs and depletion in Nb, Ta, and Ti, consistent with our results (Fig. 13c; Ayers, 1998; Plank & Langmuir, 1998). The Nb/U values of the Lut Block volcanic rocks are much lower than those of MORB and OIB (Fig. 13d), indicating that these rocks were metasomatized by subduction-related hydrous fluids. Thus, we suggest that these volcanic rocks were derived from mantle material enriched by the input of subduction-related materials.

6.3. Fc and AFC process

In the subduction zones, in addition to pure fractional crystallization, the magmas could have assimilated by arc crust during ascending. Most arc magmas have geochemical characteristics consistent with the incorporation of variable amounts of continental crust. The crustal signature can be imparted on the source by simple subduction of sediment, or by the combined effects of the composition of subducted material along with elemental

fractionations attending prograde metamorphism during the subduction (Davidson et al., 2005).

The Kuh-e-Shah volcanic rocks have low MgO (mean 3.7 wt%, Table 1) and Ni contents (mean 13 ppm; Table 1), suggesting that they do not represent primary magma composition. The concentrations of Ni and MgO in these rocks displaying a negative correlation with increasing SiO_2 content. Ni and Mg are sensitive indicators of olivine and clinopyroxene fractionation. Increasing SiO_2 and decreasing MgO (Fig. 6e) with decreasing Cr and Ni (Figs. 14a and 14b) indicate significant fractionation crystallization of olivine and clinopyroxene (e.g., Xie et al., 2007). Meanwhile, clinopyroxene fractionation is further supported by the negative correlation of SiO_2 with CaO (Fig. 6f) and Al_2O_3 with CaO/Na_2O. Moreover, the high Al_2O_3 and Sr contents, along with the similarity of chondrite normalized REE pattern (Fig. 7a) with typical arc andesites and weak Eu negative anomalies in the studied rocks, reflect minor plagioclase fractionation. All of these parameters exhibit that clinopyroxene fractionation affects the evolution of the Kuh-e-Shah volcanic rocks.

We used selected major and trace element variation, inter-element ratio diagrams, and Sr isotopic changes to model the effect of mixing, fractional crystallization, and assimilation-fractional-crystallization processes. In La vs. Nb (Fig. 14c; Szilas et al., 2015) and initial $^{87}Sr/^{86}Sr$ vs. SiO_2 diagram (Fig. 14d; Soesoo, 2000), located samples show a trend between AFC and FC process for the Kuh-e-Shah volcanic rocks that indicate insignificant contamination.

6.4. Geochronology

Based on all geochronology data done to today, magmatic activity in the Lut block started in the late Jurassic and continued into the Quaternary, forming a variety of volcanic and volcanoclastic rocks, as well as subvolcanic stocks. Jung et al. (1983) described Tertiary

magmatic rocks in the northern part of the Lut block as including a wide compositional range from basaltic to rhyolitic. These volcanic rocks erupted together during the Late Cretaceous to the early Neogene. The exposed volcanic rocks change in age from 46 Ma (Middle Eocene: SW of Dehsalm) to 24 Ma (Late Oligocene: SE of Nehbandan) based on the published data (collected by Pang et al., 2013; Fig. 1). These rocks (includes the Kuh-e-Shah complex), are regarded as Eocene-Oligocene in age, but they clearly predate the late Eocene porphyry. Volcanic rocks, as the extrusive counterparts of the mineralized intrusions, can provide important information on the magma source, petrogenesis, and metallogenic conditions of the coeval porphyry-epithermal system (Feng et al., 2020). Studies show that intrusions are slightly younger than the volcanic rocks, with an age range of 31 to 40 Ma (e.g., Karimpour et al., 2011). This time interval and the new U-Pb zircon data of the Kuh-e-Shah volcanic rocks demonstrate that the intrusive rocks intruded into older volcanic rocks (Late Eocene, Bartonian stage). This period can be considered as the onset of Tertiary magmatism in the Kuh-e-Shah complex.

6.5. Rb-Sr and Sm-Nd isotopic consequences

One of the locations in which andesites may take on the isotopic characteristics of crustal rocks is the above subduction zones, where the overlying crust is more youthful. High $^{87}Sr/^{86}Sr$ and low $^{143}Nd/^{144}Nd$ ratios cannot be derived from the mantle, indicate a contribution from subducted sedimentary material, itself derived from ancient continents. The Kuh-e-Shah intrusive (Etemadi et al., 2019) and volcanic rocks are more enriched in Sr-Nd compared with the mafic plutons (gabbros), consistent with minor crustal contamination of the parental magma. The enriched Sr-Nd–Hf isotopic features of the samples, indicate that the parental melts of the studied volcanic rocks were derived from the enriched mantle.

The small variation of the Sr and Nd isotope ratios within the rocks from the same unit can be related to the effects of crustal assimilation or magma source heterogeneity (Nabatian et al., 2014). The limited isotopic variation indicates that probably the Kuh-e-Shah volcanic rocks were barely affected by seawater alteration and the parental magmas rooted from a subduction-related magma source (Zhang et al., 2006). The horizontal trends of plotted samples in $^{87}Sr/^{86}Sr(i)$ and $^{143}Nd/^{144}Nd(i)$ versus MgO graphs (Figs. 14e and 14f) indicate that fractional crystallization was the dominate process in their magmatic evolution. On the other hand, the random variations of $^{87}Sr/^{86}Sr(i)$ and eNd(t) vs. MgO tend to suggest an insignificant effect of low contamination by crustal rocks instead of source heterogeneity.

7. Geodynamic setting and tectono-magmatic model

Iran is located in the middle part of this belt that represents the Tethys Sea. The Kuh-e-Shah volcano-plutonic complex, situated in the Lut Block of eastern Iran, and is believed was created by the subduction of the Sistan Ocean, a narrow arm of the Neo-Tethys Ocean (Camp & Griffis, 1982; Tirrul et al., 1983) that closed during the Oligocene-Miocene between the Afghan and Lut plates (Sengör & Natalin, 1996) prior to the collision of the Arabian and Asian plates (Camp & Griffis, 1982; Tirrul et al., 1983). Based on radiolarian records, it was argued that the Sistan Ocean opened during the Early Cretaceous (Babazadeh & De Wever, 2004). Although the mechanisms and final closure time of the Sistan Ocean remain poorly understood, some researchers adopt a 59-46 Ma as the end of Sistan slab subduction (Van der Meer et al., 2018). Various models of evolution are presented for this ocean, involving extensional tectonic setting (e.g. Jung et al., 1983; Tarkian et al., 1983) along with other subduction theories like eastward subduction beneath the Afghan Block (Camp & Grifs, 1982; Tirrul et al., 1983), western subduction beneath the Lut Block (Zarrinkoub et al., 2012), eastward intra-oceanic subduction (Saccani et al., 2010), two-sided subduction

(Arjmandzadeh et al., 2011), and northeastward subduction beneath the northcentral Lut Block (Saadat & Stern, 2016) have been put forward in this regard. Meanwhile, as mentioned by Karimpour et al. (2011), abundant intrusive bodies in the Lut Block might be formed under different tectonic conditions that should be considered. Regardless of the east-directed subduction evidence, the west-directed subduction support by evidence such as lower P and S seismic velocity (hotter and thicker section of asthenosphere), the greater amount of the Tertiary (Eocene to Oligocene) arc-related magma (calc-alkaline) in the central to northern parts of the Lut block and the northern parts of the SSZ zone, decreases the intrusive rocks ages from the north to the south of the Lut Block, the parallel repeated exposure of ophiolitic outcrops with the NW-SE direction in the northern part of the SSZ, and N-S direction in the border areas between the Lut Block and SSZ, capabilities and suitable targets for Cu-Au-Mo porphyry epithermal mineralization in the Lut Block, in a large scale. All of the mentioned items are similar to what is visible in the southern parts of the Urumieh-Dokhtar Magmatic Arc (UDMA), in the south of Iran. These witnesses suggest that the Sistan Ocean had branches at its northern end, and its closure starts from the north with subduction under the Lut Block. Our evidence and hypothesis are in line with those confirm subduction under the Lut Block without rejection the evidence of subduction under the Afghan block, as Van der Meer et al., 2018 identify only one slab beneath eastern Iran, the Sistan slab.

Based on geochemical and geochronology data, subduction-related magmatism in the Lut Block started with the Middle Jurassic granitoids, continued in the Late Cretaceous (granitoids), Late Paleocene (ignimbrites), Middle Eocene to Early Oligocene (the peak of magmatism; volcanics and subvolcanics) and finally ended with the eruption of Neogene oceanic island basalts from the western and eastern margins of the Lut Block. Based on the petrographic, geochemical, and geochronological data of the Kuh-e-Shah volcanic rocks, we suggest that these rocks probably resulted from the Sistan subducted oceanic crust and the

overlying mantle wedge with spinel lherzolite composition under the Lut Block during the Mesozoic and early Tertiary in a continental arc setting. The Eocene peak in volcanic activity (Paleogene) is resulted by changing subduction geometry, associated with the collision of Arabia with Iran and the closing of Neotethys, which caused hot asthenosphere to well up under the Lut Block (Saadat & Stern, 2016). A schematic template of the Kuh-e-Shah complex geodynamic setting is shown in Fig. 15 that is in line with the western subduction of the Sistan Ocean under the Lut Block and/or a two-sided subduction geometry.

8. Conclusions

In addition to the Urumieh–Dokhtar, and Alborz geological zones, eastern Iran encludes extensive Eocene–Oligocene magmatic rocks that covered over half of the Lut block and are manifestations of a Paleogene magmatic flare-up in Iran. In this study, tried to investigate and compare the petrology and geochemistry of the Lut Block volcanic rocks (andesite group) with their similar type in the Kuh-e-Shah complex which hosts several Au-Cu porphyry occurrences to examine their petrogenesis and regional tectonic implications.

The exposed volcanic rocks in the Kuh-e-Shah are mainly composed of three groups of trachy-andesites, andesites and, basaltic-andesites containing plagioclase and hornblende phenocrysts with minor biotite, olivine, and pyroxene in a porphyritic to trachytic textures. The Lut Block andesitic rocks show typical features of calc-alkaline to shoshsonitic series.

Geochemical variation along with the flat, depleted MREE-HREE profiles strongly suggest the role of pyroxene controlling REE fractionation and suppression of plagioclase crystallization. HFSE depletion versus LILE enrichment suggests a subduction-related setting. The REE geochemistry along with the Sr-Nd isotope composition shows that the volcanic rocks are related to the subduction zone of lithospheric mantle. The parent melts formed by low partial melting of the enriched mantle (spinel lherzolite composition). Fractional

crystallization along with insignificant crustal contamination is considered to be the dominant process controlling the geochemical evolution of studied andesitic rocks.

The new ages indicate that the magmatism was active from the Middle Eocene (~46 Ma) to the Late Oligocene (~25 Ma) in the Lut Block but in the Kuh-e-Shah started with the eruption of volcanic and volcaniclastic rocks during the Late Eocene (38.6 ±0.5 Ma to 38.9 ±0.6 Ma - Bartonian stage) and continued with intruding of subvolcanic rocks of the Late Eocene age that some of which are related to Au-Cu porphyry type mineralization.

Based on petrography, geochemistry, Rb-Sr isotope composition, and U-Pb zircon dating, it is concluded that the Lut Block andesitic rocks (also containing the Kuh-e-Shah volcanic rocks) formed during a period of the extensive Paleogene volcanism and resulted from subduction of Sistan oceanic crust under the Lut Block during Cretaceous in a continental arc setting.

Acknowledgments

This study is part of the first author's Ph.D. thesis and has been supported by the Research Foundation of Ferdowsi University of Mashhad, Iran, (Project No. 3.36963). The authors wish to thank the Ministry of Sciences, Research and Technology of Iran for financial support during sabbatical research of the first author in Portugal. The authors gratefully acknowledge the Lithos journal manager Dr. Parthiban Rajendran, the editor in Chief Prof. Dr. Xian-Hua Li, and constructive comments on the paper offered by the anonymous referees.

Declaration of interests

The authors declare that they have no known competing financial interests or personal relationships that could have appeared to influence the work reported in this paper.

Supplementary data

Supplementary material

References

Arjmandzadeh, R., Karimpour, M.H., Mazaheri, S.A., Santos, J.F., Medina, J.M., Homam, S.M., 2011. Sr–Nd isotope geochemistry and petrogenesis of the Chah-Shaljami granitoids (Lut block, eastern Iran). Journal of Asian Earth Sciences 41(3), 283-296.

Ayers, J., 1998. Trace element modeling of aqueous fluid-peridotite interaction in the mantle wedge of subduction zones. Contributions to Mineralogy and Petrology 132, 390–404.

Ayers, J.C., 1998. Trace element modeling of aqueous fluid–peridotite interaction in the mantle wedge of subduction zones. Contributions to Mineralogy and Petrology 132(4), 390-404.

Babazadeh, S.A., De Wever, P., 2004. Radiolarian Cretaceous age of Soulabest radiolarites in ophiolite suite of eastern Iran. Bulletin de la Société Géologique de France 175(2), 121-129.

Bagheri, S., Stampfli, G.M., 2008. The Anarak, Jandaq and Posht-e-Badam metamorphic complexes in central Iran: new geological data, relationships and tectonic implications. Tectonophysics 451(1-4), 123-155.

Baker, M.B., Hirschmann, M.M., Ghiorso, M.S., Stolper, E.M., 1995. Compositions of near-solidus peridotite melts from experiments and thermodynamic calculations. Nature 375, 308–311.

Berberian, F., Muir, I.D., Pankhurst, R.J., Berberian, M., 1982. Late Cretaceous and early Miocene Andeantype plutonic activity in northern Makran and Central Iran. Journal of the Geological Society 139, 605-614.

Berberian, M., 1977. Against the Rigidity of the Lut Block; A Seismotectonic Discussion. Geological Survey of Iran 40, 203-227.

Blatt, H., Tracy, R., Owens, B., 2006. Petrology: igneous, sedimentary and metamorphic. third ed. W.H. Freeman and company, New York.

Boynton, W.V., 1985. Cosmochemistry of the rare earth elements: meteorite studies. In developments in geochemistry, Amsterdam, Elsevier, pp. 63-114.

Brown, G.C., Thorpe, R.S., Webb, P.C., 1984. The geochemical characteristics of granitoids in contrasting arcs and comments on magma sources. Journal of the Geological Society 141(3), 413-426.

Camp, V.E., Griffis, R.J., 1982. Character, genesis and tectonic setting of igneous rocks in the Sistan suture zone, eastern Iran. Lithos 15(3), 221-239.

Chang, Z., Vervoort, J.D., McClelland, W.C., Knaak, C., 2006. U-Pb dating of zircon by LA-ICP-MS, Geochem Geophy Geosy 7: 1-14.

Chiaradia, M., Müntener, O., Beate, B., 2011. Enriched basaltic andesites from mid-crustal fractional crystallization, recharge, and assimilation (Pilavo Volcano, Western Cordillera of Ecuador). Journal of Petrology 52(6), 1107-1141.

Cotten, J., Le Dez, A., Bau, M., Caroff, M., Maury, R.C., Dulski, P., Brousse, R., 1995. Origin of anomalous rare-earth element and yttrium enrichments in subaerially exposed basalts: evidence from French Polynesia. Chemical Geology 119(1-4), 115-138.

Cox, K.G., Bell, J.D., Pankhurst, R.J., 1979. The Interpretation of Igneous Rocks. George Allen and Unwin, London, United Kingdom.

Davidson, J., Turner, S., Plank, T., 2013. Dy/Dy*: variations arising from mantle sources and petrogenetic processes. Journal of Petrology 54(3), 525-537.

Davidson, J.P., Hora, J.M., Garrison, J.M. and Dungan, M.A., 2005. Crustal forensics in arc magmas. Journal of Volcanology and Geothermal Research 140(1-3), 157-170.

Esmaeily, D., 2001. Petrology and geochronology of Shah-Kuh granite with special references to tin mineralization. Ph.D thesis, Tarbiat Modares University.

Etemadi, A., Karimpour, M.H., Shafaroudi, A.M., 2018. Geology, petrography, alteration, mineralization and petrogenesis of intrusive bodies in the Hamech prospect area,

Southwest of Birjand. Journal of Economic Geology 10(1), 113-137 (in Persian with English abstract).

Etemadi, A., Karimpour, M.H., Shafaroudi, A.M., Santos, J.F., Mathur, R., Ribeiro, S., 2019. U-Pb zircon geochronology, geochemistry, and petrogenesis of the Hamech intrusions in the Kuh-e-Shah volcano-plutonic complex, Eastern Iran. Turkish Journal of Earth Sciences 28(1), 38-59.

Feeley, T.C., Davidson, J.P., 1994. Petrology of calk-alkaline lavas at Volcan Ollague and the origin of compositional diversity at central Andean stratovolcanoes. Journal of Petrology 35, 1295–1340.

Feng, Z.Z., Bai, Z.J., Zhong, H., Zhu, W.G., Zheng, S.L., 2020. Genesis of Volcanic Rocks in the Zijinshan Ore District, SE China: Implications for Porphyry-Epithermal Mineralization. Minerals 10(2), 200.

Geological survey of iran., 1975. Geological quadrangle map of Sar-e-Chah-e-Shur (1:100,000). Sheet No. 7754.

Geological survey of iran., 1978. Geological quadrangle map of Mokhtaran (1:100,000). Sheet No. 7854.

Ghorbani, M., 2013. The economic geology of Iran: mineral deposits and natural resources. Springer Science and Business Media, Dordrecht.

Gill, J.B., 1981. Orogenic andesites and plate tectonics. Springer-Verlag, Berlin.

Gill, R., 2010. Igneous rocks and processes. Wiley-Blackwell, Malaysia.

Gudnason, J., Holm, P.M., Søager, N., Llambías, E.J., 2012. Geochronology of the late Pliocene to recent volcanic activity in the Payenia back-arc volcanic province, Mendoza Argentina. Journal of South American Earth Sciences 37, 191–201.

Hofmann, A.W., Jochum, K.P., Seufert, M., White, W.M., 1986. Nb and Pb in oceanic basalts: New constraints on mantle evolution. Earth and Planetary science letters 79, 33–45.

Hong, D., Zhang, J., Wang, T., Wang, S., Xie, X., 2004. Continental crustal growth and the supercontinental cycle: evidence from the Central Asian Orogenic Belt. Journal of Asian Earth Sciences 23(5), 799-813.

Ionov, D.A., Hofmann, A.W., 1995. Nb-Ta-rich mantle amphiboles and micas: Implications for subduction-related metasomatic trace element fractionations. Earth and Planetary Science Letters 131(3-4), 341-356.

Irvine, T.N.J., Baragar, W.R.A., 1971. A guide to the chemical classification of the common volcanic rocks. The Canadian Journal of Earth Sciences 8(5), 523-548.

Javidi Moghaddam, M., Karimpour, M.H., Malekzadeh Shafaroudi, A., Santos, J.F., Corfu, F., 2019. Middle Eocene magmatism in the Khur region (Lut Block, Eastern Iran): implications for petrogenesis and tectonic setting. International Geology Review 61, 1-16.

Jung, D., Keller, J., Khorasani, R., Marcks, C.H.R., Baumann, A., Horn, P., 1983. Petrology of the Tertiary magmatic activity the northern Lut area, East of Iran. Ministry of mines and metals, GSI, geodynamic project (geotraverse) in Iran, No. 51, 285-336.

Karimpour, M., 2011. Review of age, Rb-Sr geochemistry and petrogenesis of Jurassic to Quaternary igneous rocks in Lut Block, Eastern Iran. Geopersia 1(1), 19-54.

Kelemen, P.B., Hanghøj, K., Greene, A.R., 2003. One view of the geochemistry of subduction-related magmatic arcs, with an emphasis on primitive andesite and lower crust. Treatise on Geochemistry, Elsevier-Pergamon, Oxford.

Kelemen, P.B., Hanghoj, K., Greene, A.R., 2014. One view of the geochemistry of subduction-resecondd magmatic arcs, with an emphasis on primitive andesite and lower crust. Treatise on geochemistry 3, 593–659.

Kendall, C., Mcdonnell, J.J., Sklash, M.G., Bullen, T.D., 1995. Isotope Tracers of Water and Solute Sources in Catchments', in: Trudgill, S. T. Solute Modeling in Catchment Systems, John Wiley & Sons Ltd, Toronto.

Li, P.J., Yu, X.Q., Li, H.Y., Qiu, J.T., Zhou, X., 2013. Jurassic–Cretaceous tectonic evolution of Southeast China: Geochronological and geochemical constraints of Yanshanian granitoids. International Geology Review 55, 1202–1219.

Ludwig, K.R., 2007. Isoplot version 3.7, User's Manual. Berkeley Geochronology Center, Special Publication 4.

Malekzadeh shafaroudi, A.M., Karimpour, M.H., Stern, C.R., 2015. The Khopik porphyry copper prospect, Lut Block, Eastern Iran: geology, alteration and mineralization, fluid inclusion, and oxygen isotope studies. Ore Geology Reviews 65, 522-544.

Mcbirney, A.R., 2007. Igneous Petrology. 3rd edition, Jones and Bartlett Learning, Burlington, Canada.

Moradi, M., Karimpour, M.H., Farmer, L.G., Stern C.R., 2011. Rb-Sr & Sm-Nd Isotopic Composition, UPb-Th (zircon) Geochronology and Petrogenesis of Najmabad granodiorite batholith. Journal of Economic Geology 2(3), 127-145 (in Persian with English abstract).

Nabatian, G., Ghaderi, M., Neubauer, F., Honarmand, M., Liu, X., Dong, Y., Jiang S., Quadt A., Bernroider, M., 2014. Petrogenesis of Tarom high-potassic granitoids in the Alborz–Azarbaijan belt, Iran: Geochemical, U–Pb zircon and Sr–Nd–Pb isotopic constraints. Lithos 184, 324-345.

Nadermezerji, S., Karimpour, M.H., Malekzadeh Shafaroudi, A., Santos, J.F., Mathur, R., Ribeiro, S., 2018. U–Pb geochronology, Sr–Nd isotopic compositions, geochemistry and petrogenesis of Shah Soltan Ali granitoids, Birjand, Eastern Iran. Chemie der erde-geochemistry 78(3), 299-313.

Pang, K.N., Chung, S.L., Zarrinkoub, M.H., Khatib, M.M., Mohammadi, S.S., Chiu, H.Y., Chu, C.H., Lee, H.Y., Lo, C.H., 2013. Eocene–Oligocene post-collisional magmatism in the Lut–Sistan region, eastern Iran: magma genesis and tectonic implications. Lithos 180, 234-251.

Pearce, J.A., 1983. Role of the sub-continental lithosphere in magma genesis at active continental margins. In: Hawkesworth, C.J., Norry, M.J. (Eds.), Continental Basalts and Mantle Xenoliths, Shiva Publisher, Nantwich, United Kingdom.

Peccerillo, A., Taylor, S.R., 1976. Geochemistry of Eocene calc-alkaline volcanic rocks from the Kastamonu area, northern Turkey. Contributions to Mineralogy and Petrology 58(1), 63-81.

Plank, T., Langmuir, C.H., 1998. The chemical composition of subducting sediment and its consequences for the crust and mantle. Chemical Geology 145(3-4), 325-394.

Plank, T.; Langmuir, C.H., 1998. The chemical composition of subducting sediment and its consequences for the crust and mantle. Chemical geology 145, 325–394.

Richards, J.P., Spell, T., Rameh, E., Razique, A., Fletcher, T., 2012. High Sr/Y magmas reflect arc maturity, high magmatic water content, and porphyry Cu±Mo±Au potential: Examples from the Tethyan arcs of central and eastern Iran and western Pakistan. Ecological geology 107(2), 295-332.

Rudnick, R.L., Fountain, D.M., 1995. Nature and composition of the continental crust: a lower crustal perspective. Reviews of geophysics 33, 267–309.

Rudnick, R.L., Gao, S., 2014. Composition of the Continental Crust. In Treatise on Geochemistry. Elsevier, Amsterdam, The Netherlands.

Rutter, M.J.; Wyllie, P.J., 1988. Melting of vapour-absent tonalite at 10 kbar to simulate dehydration-melting in the deep crust. Nature 331, 159-160.

Saadat, S., Stern, C., 2016. Distribution and geochemical variations among paleogene volcanic rocks from the north-central Lut block, eastern Iran. Iranian Journal of Earth Sciences (IJES) 8(1), 1-24.

Saccani, E., 2014. A new method of discriminating different types of post-Archean ophiolitic basalts and their tectonic significance using Th-Nb and Ce-Dy-Yb systematics. Geoscience Frontiers 6(4), 481-501.

Saccani, E., Delavari, M., Beccaluva, L., Amini, S., 2010. Petrological and geochemical constraints on the origin of the Nehbandan ophiolitic complex (eastern Iran): Implication for the evolution of the Sistan Ocean. Lithos 117(1-4), 209-228.

Samiee, S., Karimpour, M.H., Ghaderi, M., Shahri, M.R.H., Klöetzli, U., Santos, J.F., 2016. Petrogenesis of subvolcanic rocks from the Khunik prospecting area, south of Birjand, Iran: Geochemical, Sr–Nd isotopic and U–Pb zircon constraints. Journal of Asian Earth Sciences 115, 170-182.

Schmidt, M.W., Jagoutz, O., 2017. The global systematics of primitive arc melts. Geochemistry, Geophysics, Geosystems 18, 2817–2854

Sengör, A.M.C., Natalin, B.A., 1996. Paleotectonics of Asia: fragment of a synthesis. In: Yin, An, Harrison, T.M. (Eds.), The Tectonic Evolution of Asia, Cambridge University Press, Cambridge.

Shaw, D.M., 1970. Trace element fractionation during anatexis. Geochimica et Cosmochimica Acta 34(2), 237-243.

Sigurdsson, H., Houghton, B., McNutt, S., Rymer, H., Stix, J., 2015. The encyclopedia of volcanoes. Elsevier.

Soesoo, A., 2000. Fractional crystallization of mantle derived melts as a mechanism for some I type granite petrogenesis: an example from Lachlan Fold Belt, Australia. Journal of the geological Society 157(1), 135-149.

Stöcklin, J., 1968. Structural history and tectonics of Iran: a review. AAPG bulletin 52(7), 1229-1258.

Stöcklin, J., Eftekhar-nezhad, J., Hushmand-zadeh, A., 1965. Geology of the Shotori range (Tabas area, east Iran), Geological Survey of Iran.

Stöcklin, J., Ruttner, A., Nabavi, M.H., 1972. New data on the Lower Paleozoic and Pre-cambrian of North Iran, Geological Survey of Iran.

Sun, S.S., Mcdonough, W.F., 1989. Chemical and isotopic systematics of oceanic basalts: implications for mantle composition and processes. Geological Society, London, Special Publications 42(1), 313-345.

Szilas, K., Hoffmann, J.E., Hansmeier, C., Hollis, J.A., Münker, C., Viehmann, S., Kasper, H.U., 2015. Sm-Nd and Lu-Hf isotope and trace-element systematics of Mesoarchaean amphibolites, inner Ameralik fjord, southern West Greenland. Mineralogical Magazine 79(4), 857-876.

Tarkian, M., Lotfi, M., Baumann, A., 1983. Tectonic, magmatism and the formation of mineral deposits in the central part, east Iran. Ministry of mines and metals, GSI, geodynamic project (geotraverse) in Iran, No. 51, 357-383.

Tepper, J.H., Nelson, B.K., Bergantz, G.W., Irving, A.J., 1993. Petrology of the Chilliwack batholith, North Cascades, Washington: generation of calc-alkaline granitoids by melting of mafic lower crust with variable water fugacity. Contributions to Mineralogy and Petrology 113(3), 333-351.

Thiéblemont, D., Tegyey, M., 1994. Geochemical discrimination of differentiated magmatic rocks attesting for the variable origin and tectonic setting of calc-alkaline magmas. Comptes rendus de l'académie des sciences 319(1), 87-94.

Tirrul, R., Bell, I.R., Griffis, R.J., camp, V.E., 1983. The Sistan suture zone of eastern Iran. Geological Society of America Bulletin 94(1), 134-150.

Van der Meer, D.G., Van Hinsbergen, D.J.J., Spakman, W., 2018. Atlas of the underworld: Slab remnants in the mantle, their sinking history, and a new outlook on lower mantle viscosity, Tectonophysics 723, 309-448.

Walker, R.T., Gans, P., Allen, M.B., Jackson, J., Khatib, M., Marsh, N., Zarrinkoub, M., 2009. Late Cenozoic volcanism and rates of active faulting in eastern Iran. Geophysical Journal International 177(2), 783-805.

Whitney, D.L., Evans, B.W., 2010. Abbreviations for names of rock-forming minerals. American Mineralogist 95(1), 185-187.

Wilson, M., 1989. Igneous Petrogenesis. Chapman and Hall, London.

Zarrinkoub, M.H., Pang, K.N., Chung, S.L., Khatib, M.M., Mohammadi, S.S., Chiu, H.Y., Lee, H.Y., 2012. Zircon U–Pb age and geochemical constraints on the origin of the Birjand ophiolite, Sistan suture zone, eastern Iran. Lithos 154, 392-405.

Zhang, H.F., Zhang, L., Harris, N., Jin, L.L., Yuan, H., 2006. U–Pb zircon ages, geochemical and isotopic compositions of granitoids in Songpan-Garze fold belt, eastern Tibetan Plateau: constraints on petrogenesis and tectonic evolution of the basement. Contributions to Mineralogy and Petrology 152(1), 75-88.

Zheng, Y.F., 2019. Subduction zone geochemistry. Geoscience Frontiers 10(4), 1223-1254.

Table 1. Major (Wt. %), trace, and rare earth element (ppm) composition of the Kuh-e-Shah volcanic rocks. Eu*: expected concentration by interpolating between the normalized value of Sm and Gd. N: normalized by REE chondrite (Boynton, 1985). Eu/Eu* = Eu/√Sm × Gd. Abbreviations: Tr-andesite: Trachy-andesite, Ba-andesite: Basaltic-andesite, LOI: Lost On Ignition.

Sample	15 E	21 E	26 E	28 E	41 S	81 S	83 E
Longitude	58° 52 29.9″	58° 50 35.8″	58° 55 44.2″	58° 54 41.1″	58° 58 23.3″	59° 07 06.8″	58° 53 21.8″

Latitude	32 24 32.3	32 21 18.5	32 24 58.7	32 25 04.8	32 21 58.2	32 22 08.3	32 22 33.2
Petrology	Tr-Andesite	Tr-Andesite	Tr-Andesite	Andesite	Andesite	Andesite	Andesite
[Wt.%]							
SiO_2	60.08	60.13	58.71	62.70	57.54	59.79	61.23
TiO_2	0.64	0.64	0.54	0.62	0.63	0.54	0.52
Al_2O_3	16.07	15.60	14.74	15.43	15.52	15.23	15.94
FeO^t	5.56	5.54	6.03	5.58	6.98	5.85	6.00
MnO	0.09	0.09	0.13	0.06	0.14	0.11	0.12
MgO	1.74	3.16	4.27	0.76	3.42	2.76	2.00
CaO	6.18	4.87	4.76	4.38	6.99	5.77	6.21
Na_2O	3.37	3.22	3.25	2.96	2.57	2.63	2.84
K_2O	3.83	4.13	3.26	3.70	2.62	2.37	2.70
P_2O_5	0.39	0.35	0.28	0.32	0.37	0.32	0.34
LOI	1.80	2.03	3.83	2.90	3.0	4.43	1.91
SUM	99.75	99.76	99.80	99.41	9	99.80	99.81
[ppm]							
Ba	789	748	643	752	41	598	565
Rb	96.1	97.8	73.1	101.2	53.7	46.7	53.5
Sr	1027.5	887.4	646.8	918.6	790.7	847.5	733.0
Zr	110.2	110.3	79.1	112.1	72.6	80.6	76.7
Nb	5.1	5.2	2.9	5.1	3.2	2.3	2.5
Ni	13	17	14	11	12	7	12
Co	16.4	13.1	13.3	12.4	15.1	11.2	11.3
Zn	73	71	8	57	71	78	66
Cr	10	29	27	16	13	8	21
Y	18.7	16.5	15.6	15.9	17.1	16.9	17.0
Cs	4.5	3.7	7.0	8.4	2.2	3.8	2.6
Ta	0.4	0.4	0.2	0.3	0.2	0.1	0.2
Hf	2.9	3.2	2.3	2.8	2.0	2.3	1.9
La	26.5	26.8	19.6	28.4	18.0	18.7	18.8
Ce	52.5	53.3	40.4	53.2	34.2	34.5	35.5
Pr	6.54	6.12	4.64	6.39	4.40	4.51	4.31
Nd	26.0	25.9	19.3	26.3	17.8	18.0	18.3
Sm	4.93	5.25	4.00	4.97	3.85	4.31	4.16
Eu	1.37	1.28	1.14	1.39	1.26	1.11	1.21
Gd	4.33	4.35	3.92	4.33	3.87	3.38	3.90
Tb	0.62	0.59	0.49	0.55	0.55	0.48	0.52
Dy	3.62	3.18	2.99	3.27	3.49	2.98	3.05
Ho	0.65	0.65	0.58	0.66	0.68	0.61	0.59
Er	1.85	1.83	1.76	1.72	2.05	1.97	1.83
Tm	0.31	0.27	0.27	0.27	0.30	0.29	0.27
Yb	2.23	1.94	1.85	1.65	2.08	2.00	2.03
Lu	0.34	0.29	0.27	0.28	0.31	0.29	0.28
$(La/Yb)_N$	8.01	9.31	7.14	11.60	5.83	6.30	6.24
$(Ce/Yb)_N$	6.09	6.71	5.65	8.34	4.25	4.46	4.52
$(Nb/Zr)_N$	0.73	0.74	0.58	0.71	0.69	0.45	0.51
Eu/Eu*	0.91	0.82	0.88	0.92	0.99	0.89	0.92

Table. (Continued).

Sample	33 N	89 N	111 S	118 N	125 N	92 N	136 N	162 N
Longitude	58° 57′ 41.5″	58° 54′ 52.9″	59° 01′ 46.6″	59° 03′ 48.2″	58° 58′ 56.6″	58° 59′ 39.2″	58° 57′ 10.9″	59° 02′ 41.2″
Latitude	32° 26′ 09.4″	32° 29′ 19.2″	32° 20′ 55.1″	32° 26′ 16.5″	32° 28′ 02.1″	32° 29′ 16.4″	32° 27′ 53.2″	32° 27′ 07.7″
Petrology	Tr-Andesite	Tr-Andesite	Tr-Andesite	Tr-Andesite	Tr-Andesite	Ba-andesite	Ba-andesite	Ba-andesite
[Wt.%]								
SiO_2	59.33	55.59	54.59	58.56	53.08	53.86	53.2	54.11
TiO_2	0.61	0.61	0.75	0.57	0.75	0.76	0.7	0.73
Al_2O_3	16.14	15.47	15.05	14.29	15.41	14.3	14.53	15.02
FeO^t	5.71	7.15	8.83	5.46	8.68	9.18	8.26	8.4
MnO	0.08	0.15	0.10	0.11	0.28	0.12	0.12	0.13
MgO	3.48	5.81	5.14	3.28	5.62	5.48	5.40	4.22
CaO	4.82	4.47	5.6	5.74	6.13	7.49	9.18	8.96
Na_2O	3.4	3.25	2.84	2.88	2.38	2.41	2.12	2.14
K_2O	3.9	3.16	3.43	4.11	3.61	2.74	2.79	3.05
P_2O_5	0.42	0.26	0.30	0.29	0.3[illegible]	0.44	0.25	0.26
LOI	1.83	3.86	3.17	4.48	3.51	3.02	3.09	2.50
SUM	99.72	99.78	99.80	99.77	99.7[illegible]	99.8	99.64	99.52
[ppm]								
Ba	809	782	709	684	11[illegible]9	561	605	670
Rb	93.4	64.1	72.9	101.[illegible]	54.2	35.9	50.6	50.2
Sr	996.6	856.6	652.9	7[illegible]86	671.2	764.9	1809.9	701.8
Zr	105.3	84.2	60.7	03.8	70.5	62.1	60.9	59.3
Nb	4.8	3.1	2.5	4.9	2.5	2.2	1.7	1.9
Ni	16	16	5	13	9	15	26	18
Co	14.2	18	23.5	15.9	18	22.7	24.9	24
Zn	82	85	9[illegible]	80	73	91	71	84
Cr	22	17	1[illegible]	23	33	53	59	47
Y	33.0	24.2	[illegible]7.5	34.0	20.1	19.3	18.7	20.5
Cs	2.8	2.8	14.1	8.1	2.0	0.9	1.6	0.6
Ta	0.4	0.2	0.1	0.4	0.2	0.2	0.1	0.1
Hf	3.1	[illegible].3	1.7	2.8	1.9	1.8	1.9	1.7
La	26.4	20.[illegible]	14.5	24.1	14.1	16.9	13.3	14.4
Ce	52.5	40.[illegible]	28.4	45.2	25.8	35.5	23.1	26.5
Pr	6.10	5.09	3.80	5.45	3.45	4.70	3.21	3.55
Nd	24.2	21.9	16.5	21.6	14.5	20.2	13.8	15.7
Sm	5.00	4.84	3.54	4.38	3.19	4.36	3.19	3.62
Eu	1.33	1.16	1.07	1.12	1.02	1.19	0.91	0.99
Gd	4.22	4.03	3.53	3.75	3.41	3.94	3.11	3.27
Tb	0.56	0.58	0.53	0.47	0.53	0.60	0.47	0.52
Dy	3.34	3.74	3.31	2.91	2.97	3.50	2.83	3.17
Ho	0.62	0.74	0.66	0.53	0.68	0.71	0.58	0.7
Er	1.90	2.13	2.00	1.68	1.96	2.15	1.84	1.86
Tm	0.30	0.30	0.31	0.21	0.29	0.32	0.26	0.27
Yb	1.86	2.08	1.95	1.59	1.88	2.09	1.83	1.96
Lu	0.31	0.31	0.29	0.26	0.28	0.31	0.29	0.31
$(La/Yb)_N$	9.57	6.52	5.01	10.22	5.06	5.45	4.90	4.95
$(Ce/Yb)_N$	7.30	5.00	3.77	7.35	3.55	4.39	3.27	3.50

$(Nb/Zr)_N$	0.72	0.58	0.65	0.74	0.56	0.56	0.44	0.50
Eu/Eu*	0.89	0.80	0.93	0.84	0.95	0.88	0.88	0.88

Table 2. The results of U-Pb zircon dating from trachy-andesite (118N) and andesite (28E) samples. Explanation: resulted mean age for these samples are taken from 32 and 34 coherent groups of zircons, Respectively.

Sample No.	U [ppm]	Th [ppm]	U/Th [ppm]	$^{207}Pb/^{235}U$	Error (2s)	$^{206}Pb/^{238}U$	Error (2s)	Corr. Coef.	Best Age Ma	Error (2s)	Discor. (%)
118N (Trachy-andesite)											
118-1	224	113.8	2.0	0.03701	0.00382	0.00583	0.00016	0.680	37.5	1.6	15.7
118-2	322	111.3	2.9	0.07665	0.00963	0.00576	0.00050	0.704	37.0	2.5	7.5
118-3	412	236.0	1.7	0.03759	0.00284	0.00616	0.00021	0.754	39.6	1.8	16.3
118-4	288	147.0	2.0	0.03998	0.00355	0.00600	0.00028	0.717	38.6	1.8	15.0
118-5	164	87.1	1.9	0.03024	0.00407	0.00607	0.00031	0.667	38.9	2.0	20.0
118-6	807	346.1	2.3	0.04033	0.00253	0.00604	0.00025	0.805	38.8	1.6	14.9
118-8	452	234.5	1.9	0.04804	0.00438	0.00609	0.00035	0.765	39.2	2.2	12.6
118-9	219	80.2	2.7	0.03719	0.00389	0.00619	0.00030	0.687	39.8	1.9	16.6
118-10	523	234.0	2.2	0.03904	0.00276	0.00629	0.00028	0.786	40.4	1.8	16.1
118-11	712	250.4	2.8	0.04920	0.00363	0.00608	0.00033	0.828	39.1	2.1	12.3
118-12	298	105.5	2.8	0.03811	0.00351	0.00594	0.00031	0.737	38.2	2.0	15.5
118-13	276	115.8	2.4	0.03851	0.00348	0.00611	0.00028	0.712	39.2	1.8	15.8
118-14	323	118.2	2.7	0.04446	0.00388	0.00593	0.00029	0.733	38.1	1.9	13.3
118-15	870	344.6	2.5	0.03853	0.00235	0.00600	0.00019	0.746	38.6	1.3	15.5
118-16	247	93.1	2.7	0.03944	0.00398	0.00614	0.00028	0.687	39.5	1.8	15.5
118-18	166	77.7	2.1	0.03905	0.00433	0.00607	0.00029	0.677	39.0	1.8	15.5
118-19	322	298.9	1.1	0.04564	0.00548	0.00595	0.00027	0.671	38.2	1.7	13.0
118-20	185	94.4	2.0	0.04375	0.00528	0.00603	0.00046	0.758	38.8	3.0	13.7
118-21	604	251.1	2.4	0.04182	0.00314	0.00574	0.00025	0.751	36.9	1.6	13.7
118-22	536	224.3	2.4	0.03908	0.00367	0.00609	0.00040	0.803	39.1	2.6	15.5
118-23	399	175.6	2.3	0.04533	0.00508	0.00631	0.00035	0.697	40.6	2.3	13.9
118-24	272	97.3	2.8	0.03787	0.00312	0.00587	0.00027	0.735	37.8	1.7	15.5
118-25	570	227.9	2.5	0.04437	0.00293	0.00614	0.00028	0.819	39.4	1.8	13.8
118-26	614	237.8	2.6	0.04001	0.00313	0.00618	0.00033	0.803	39.7	2.1	15.4
118-28	559	275.9	2.0	0.06763	0.00543	0.00931	0.00054	0.823	59.7	3.4	13.7
118-30	280	123.6	2.3	0.03761	0.00385	0.00586	0.00034	0.732	37.6	2.2	15.5
118-31	342	99.3	3.4	0.03989	0.00332	0.00612	0.00030	0.747	39.3	1.9	15.3
118-33	217	84.6	2.6	0.03325	0.00425	0.00640	0.00040	0.690	41.1	2.6	19.2
118-34	242	100.5	2.4	0.03388	0.00467	0.00574	0.00039	0.692	36.9	2.5	16.9
118-35	1163	389.7	3.0	0.03732	0.00269	0.00581	0.00028	0.794	37.3	1.8	15.5
118-36	187	73.7	2.5	0.05615	0.00570	0.00598	0.00035	0.729	38.5	2.2	10.6
118-37	454	208.3	2.2	0.03622	0.00296	0.00606	0.00032	0.786	38.9	2.1	16.7
118-38	686	253.0	2.7	0.04653	0.00335	0.00592	0.00030	0.812	38.0	1.9	12.7
28E (Andesite)											

28-1	407	162	2.5	0.04097	0.00337	0.00622	0.00027	0.724	39.9	1.8	15.1
28-2	273	112	2.4	0.07253	0.00548	0.00627	0.00028	0.739	40.3	1.7	8.6
28-3	211	78	2.7	0.03147	0.00326	0.00598	0.00028	0.686	38.4	1.8	19.0
28-4	410	152	2.7	0.03893	0.00319	0.00597	0.00025	0.716	38.4	1.6	15.3
28-5	197	67	2.9	0.03900	0.00365	0.00594	0.00028	0.703	38.2	1.8	15.2
28-6	151	73	2.1	0.04488	0.00618	0.00606	0.00033	0.666	39.0	2.1	13.5
28-7	550	204	2.7	0.03865	0.00267	0.00601	0.00024	0.753	38.6	1.5	15.5
28-8	1291	317	4.1	0.03874	0.00217	0.00591	0.00021	0.807	38.0	1.4	15.2
28-9	120	52	2.3	0.04005	0.00581	0.00623	0.00033	0.665	40.0	2.2	15.5
28-10	349	141	2.5	0.03722	0.00309	0.00600	0.00025	0.712	38.5	1.6	16.1
28-11	158	48	3.3	0.04090	0.00434	0.00609	0.00030	0.687	39.1	1.9	14.8
28-12	448	193	2.3	0.05048	0.00435	0.00593	0.00034	0.778	38.1	2.1	11.7
28-13	133	62	2.1	0.10352	0.00975	0.00623	0.00039	0.755	40.0	2.3	6.0
28-14	1302	440	3.0	0.03748	0.00263	0.00577	0.00027	0.799	37.1	1.7	15.3
28-15	211	91	2.3	0.03980	0.00387	0.00622	0.00031	0.707	39.9	2.0	15.6
28-16	162	87	1.9	0.04395	0.00525	0.00613	0.00034	0.684	39.4	2.2	13.9
28-17	173	81	2.1	0.03987	0.00503	0.00590	0.00032	0.675	37.9	2.1	14.8
28-18	625	320	2.0	0.03899	0.00252	0.00601	0.00022	0.759	38.6	1.4	15.4
28-19	589	233	2.5	0.04239	0.00274	0.00608	0.00023	0.763	39.1	1.5	14.3
28-20	871	285	3.1	0.04144	0.00252	0.00624	0.00023	0.776	40.1	1.5	15.0
28-21	450	182	2.5	0.04801	0.00310	0.00600	0.00023	0.766	38.6	1.5	12.5
28-22	728	296	2.5	0.03834	0.00220	0.00593	0.00020	0.781	37.5	1.3	15.2
28-23	186	93	2.0	0.04317	0.00480	0.00612	0.00028	0.676	39.3	1.8	14.1
28-24	201	162	1.2	0.03742	0.00410	0.00610	0.00024	0.676	39.2	1.6	16.3
28-25	201	71	2.8	0.05085	0.00547	0.00623	0.00030	0.681	40.0	1.9	12.2
28-26	415	162	2.6	0.03754	0.00277	0.00600	0.00025	0.749	38.6	1.6	15.9
28-27	626	200	3.1	0.03669	0.00253	0.00585	0.00024	0.764	37.6	1.6	15.9
28-28	257	113	2.3	0.03575	0.00371	0.00602	0.00028	0.686	38.7	1.8	16.8
28-29	603	240	2.5	0.04143	0.00315	0.00581	0.00026	0.756	37.4	1.7	14.0
28-30	148	78	1.9	0.03673	0.00523	0.00600	0.00034	0.666	38.6	2.2	16.3
28-31	168	77	2.2	0.03957	0.00482	0.00599	0.00031	0.673	38.5	2.0	15.5
28-32	295	144	2.1	0.03701	0.00325	0.00571	0.00023	0.695	36.7	1.5	15.4
28-33	219	90	2.4	0.03907	0.00378	0.00612	0.00030	0.707	39.4	1.9	15.6
28-34	216	80	2.7	0.03922	0.00427	0.00629	0.00030	0.680	40.4	1.9	16.0

Individual errors are given as 2 sigma standard deviation and only reflect the internal error, Systematic or external error are $^{206}Pb/^{238}U$ = 1.2%, $^{207}Pb/^{206}Pb$ = 0.7% (2s). Discor. : Discordance (absolute value of the differences between $^{206}Pb/^{238}U$ and $^{207}Pb/^{235}U$ dates) = [1-($^{206}Pb/^{238}U/^{207}Pb/^{235}U$)] × 100.

Table 3. Rb-Sr and Sm-Nd isotopic data for eleven whole-rock samples of the Kuh-e-Shah volcanic rocks. Initial $^{87}Sr/^{86}Sr$ and $^{143}Nd/^{144}Nd$ ratios were calculated using the crystallization age of 38.6 Ma (based on new geochronological data).

Ref. No.	Lithology	$^{87}Rb/^{86}Sr$ sample	$^{87}Sr/^{86}Sr$ measured	$(^{87}Sr/^{86}Sr)$ initial	$^{147}Sm/^{144}Nd$ sample	$^{143}Nd/^{144}Nd$ measured	$(^{143}Nd/^{144}Nd)$ initial	$(\varepsilon Nd)i$	TDM (Ga)
28 E	Andesite	0.319	0.704994	0.704820	0.114	0.512651	0.512622	0.67	0.62
41 S	Andesite	0.196	0.704732	0.704625	0.131	0.512732	0.512699	2.15	0.59
83 E	Andesite	0.211	0.704789	0.704673	0.138	0.512743	0.512708	2.33	0.62
15 E	Trachy andesite	0.271	0.704936	0.704788	0.115	0.512704	0.512675	1.68	0.54
21 E	Trachy andesite	0.319	0.704939	0.704765	0.123	0.512650	0.512619	0.60	0.67
33 N	Trachy-andesite	0.271	0.704945	0.704795	0.125	0.512688	0.512657	1.34	0.63
111 S	Trachy-andesite	0.323	0.704662	0.704484	0.130	0.512812	0.512779	3.73	0.45
125 N	Trachy-andesite	0.234	0.704587	0.704458	0.133	0.512799	0.512765	3.45	0.49
92 N	Basaltic-andesite	0.136	0.704425	0.704350	0.131	0.512807	0.512774	3.63	0.46
136 N	Basaltic-andesite	0.109	0.704582	0.704522	0.134	0.512755	0.512721	2.59	0.57
162 N	Basaltic-andesite	0.207	0.704605	0.704491	0.139	0.512813	0.512778	3.71	0.50

Explanation: Errors are in 2σ, i: initial ratios. To calculate the $^{87}Rb/^{86}Sr$ and $^{147}Sm/^{144}Nd$ errors, it is assumed, in providing concentrations the following errors: 10% for values less than 1ppm, 5% for values less than 10 ppm and 2% for the remaining concentrations.

Fig.1. a) Simplified structural-geological map of Iran, indicator the location of Lut and Tabas Blocks in Central Iranian Micro continent (CIM). b) Regional geological map of Tabas Block (TB), Lut Block (LB), and East Iranian Ranges (EIR; also known as Eastern Iran Flysch zone). in both parts (a and b), the green box shows the western part of the Kuh-e-Shah volcano-plutonic complex, study area.

Fig.2. Field photographs of rocks outcrop in the Kuh-e-Shah volcano-plutonic complex. a) Remote view of subvolcanic intrusions outcrop (mostly with intermediate composition) in heights and volcanic rocks in low altitudes and plain (view to the south), b) Altered intrusive rocks outcrop, c) Exposed part of the volcaniclastic units in the Kuh-e-Shah southern slope, d)

Volcanic rocks outcrop (north of study area), e and f) Volcanic rocks outcrop (east to southeast of the study area).

Fig.3. Geological map of the western part of the Kuh-e-Shah volcano-plutonic complex, study area. Geological information adapted from the Sar-e-Chah-e-Shur and Mokhtaran 1:100000 geological sheets (Geological Survey of Iran, 1975; 1978)

Fig.4. Microscopic images together with remarkable observation during petrographic studies of the Kuh-e-Shah volcanic units in cross-polarized light (XPL). a) Porphyritic texture, b) Zoning in some plagioclase, c) Hornblende andesite, d) Reaction rims around plagioclase and pyroxenes phenocrysts, e) Opasitization of hornblende, f) Trachy-andesite, g) Biotite-hornblende andesite, h) Pyroxene-hornblende andesite, i) Alteration of olivines minerals to serpentine, Fe-oxide and partially replaced by chlorite and opaque mineral assemblages. (Px = Pyroxene, Pl = Plagioclase, Hbl = Hornblende Bt = Biotite, Chl = Chlorite, Ol = Olivine, Srp = Serpentine and Op = Opaque minerals; abbreviation of minerals derived from Whitney & Evans, 2010).

Fig.5. a) Classification of the Kuh-e-Shah volcanic rocks according to Cox et al., (1979). b) AFM diagram of Irvine and Baragar (1971) including tholeiitic and calc-alkaline magmatic differentiation trends, c) Total alkali-silica (TAS) chemical classification diagram of the Kuh-e-Shah volcanic rocks, retrieved from Peccerillo and Taylor (1976).

Fig. 6. Bivariate plots of SiO_2 (as an index of fractionation) versus selected major oxides for the Kuh-e-Shah volcanic rocks.

Fig.7. a) Chondrite-normalized diagram for the Kuh-e-Shah volcanic rocks, normalized values are from Boynton (1985), b) PM (Primitive mantle) normalized multi-element patterns for the Kuh-e-Shah volcanic rocks. PM normalizing values are from Sun and McDonough, 1989.

Fig.8. $(Nb/Zr)_N$ versus Zr diagram (Thiéblemont & Tegyey, 1994); Nb/Zr ratio normalized to the primitive mantle (average from Sun & McDonough, 1989).

Fig.9. Representative cathodoluminescence (CL) images of trachy-andesite (a; 118 N) and andesite (b; 28 E) zircons from the Kuh-e-Shah volcanic rocks. The red circles show the position of U-Pb analytical spots with corresponding $^{207}Pb/^{206}Pb$ ages.

Fig.10. U-Pb Concordia diagrams and weighted average plots for zircons extracted from selected samples. a and c) TuffZirc plot showing zircon ages for the trachy-andesite (118 N) and andesite (28 E) zircons, b and d) Tera-Wasseburg Concordia diagrams of the trachy-andesite (118 N) and andesite (28 E) zircons.

Fig.11. εNd(i) vs. $(^{87}Sr/^{86}Sr)i$ diagram for the Kuh-e-Shah volcanic rocks. Initial $^{143}Nd/^{144}Nd$ and $^{87}Sr/^{86}Sr$ ratios were calculated using the crystallization age of 38.6 Ma.

Fig.12. a) Zr/Y vs. Zr diagram to distinguish between oceanic and continental volcanic arc settings (Pearce, 1983), b) Rb/Zr versus Nb diagram (Brown et al., 1984) to determine the magma source environment and arc maturity, and c) Th_N vs. Nb_N diagram (after Saccani, 2014) showing tectonically affiliated to an active continental margin volcanic arc with polygenetic crustal signatures for studied samples. OCTZ: Oceanic-Continent Transition

Zone. Nb and Th are normalized to the Primitive Mantle (PM) composition of Sun and McDonough (1989).

Fig.13. a) The whole rock Ba/Nb versus La/Nb (Li et al., 2013). All of the volcanic rocks of Lut Block plot in the arc volcanics with this difference that the Kuh-e-Shah volcanic rocks located far from the continental crust average, may due to insignificant contamination, b) Sm/Yb versus La/Sm diagram to determine the origin of the Kuh-e-Shah volcanic rocks (Shaw, 1970), c) The whole rock Nb/U versus ($^{87}Sr/^{86}Sr$)i. Data for globally subducted sediment and slab-derived fluid are from Ayers, 1998 and Plank & Langmuir, 1998, d) The whole rock Nb/U versus Nb. The regions between the dashed lines are from Hofmann et al., 1986 and Rudnick & Gao, 2014.

Fig.14. Plots of (a) Ni vs. SiO_2 and (b) Cr vs. SiO_2 for the Kuh-e-Shah volcanic rocks. c) La vs. Nb (Szilas et al., 2015) and d) initial $^{87}Sr/^{86}Sr$ vs. SiO_2 diagram (Soesoo, 2000), to show a differentiation between AFC and FC process. e and f) The MgO versus $^{87}Sr/^{86}Sr(i)$ and $^{143}Nd/^{144}Nd(i)$ diagrams to determine the effective process in the magmatic evolution of the Kuh-e-Shah volcanic rocks. e) The MgO versus $^{87}Sr/^{86}Sr(i)$ diagram, and f) The MgO versus $^{143}Nd/^{144}Nd(i)$ diagram. All of the Kuh-e-Shah volcanic rocks show the same trend compatible with fractional crystalization.

Fig.15. Schematic tectonic model suggesting the westward subduction of the Sistan oceanic crust under the Lut Block during the Mesozoic and early Tertiary. See text for discussion.

Highlights

- *Geochemistry and geochronology of the Kuh-e-Shah volcano-plutonic complex in E Iran.*
- *Late Eocene volcanic rocks are andesitic to rhyodacitic tuffs and breccias.*
- *Chemistry compatible with origin above a subduction zone.*

- *Data show an active continental margin beneath Lut Block in E Iran during Palaeogene.*

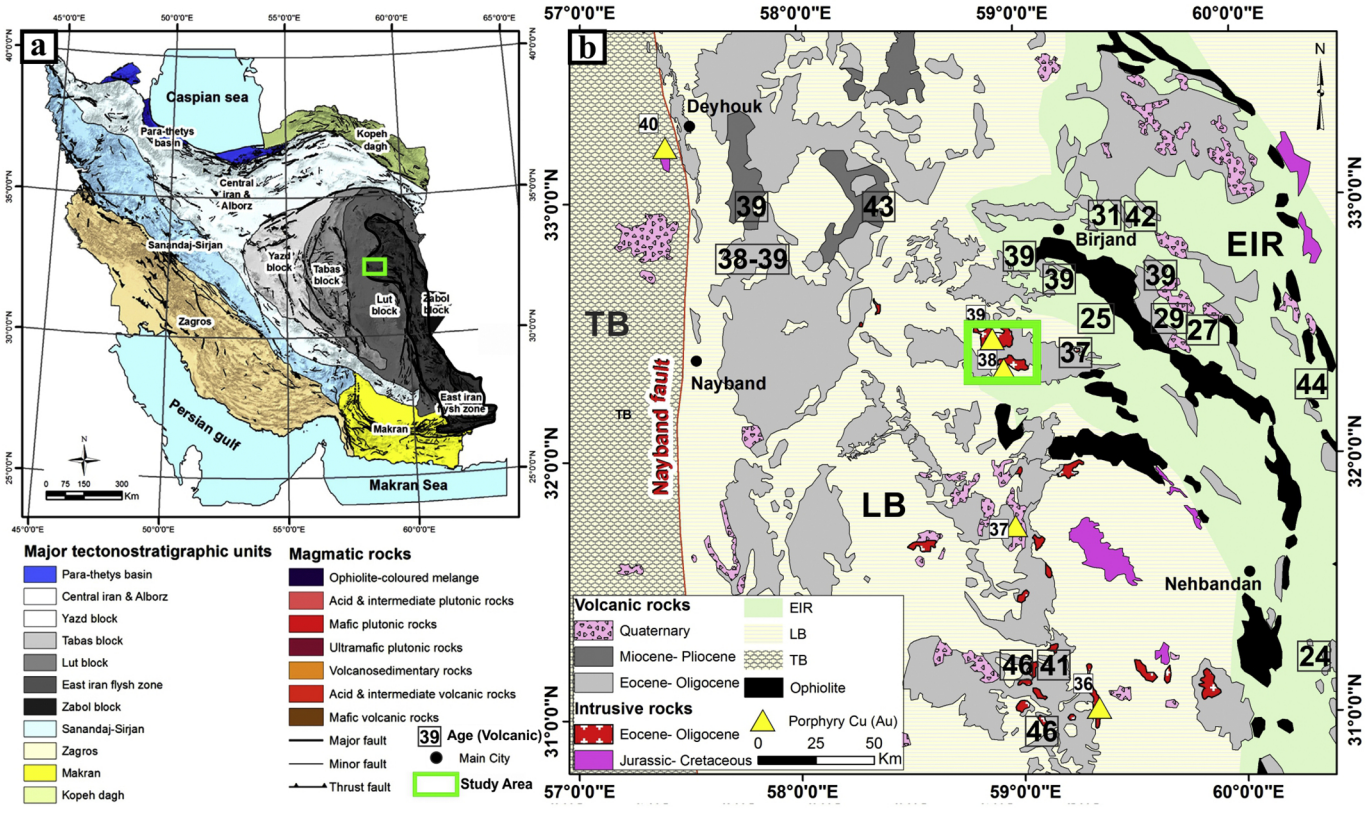
a
Caspian sea
Para-thetys basin
Kopeh dagh
Central Iran & Alborz
Sanandaj-Sirjan
Yazd block
Tabas block
Lut block
Zabol block
Zagros
East iran flysh zone
Makran
Persian gulf
Makran Sea
0 75 150 300 Km
b
Deyhouk
Nayband
Nayband fault
TB
LB
EIR
Birjand
Nehbandan
Major tectonostratigraphic units
Para-thetys basin
Central iran & Alborz
Yazd block
Tabas block
Lut block
East iran flysh zone
Zabol block
Sanandaj-Sirjan
Zagros
Makran
Kopeh dagh
Magmatic rocks
Ophiolite-coloured melange
Acid & intermediate plutonic rocks
Mafic plutonic rocks
Ultramafic plutonic rocks
Volcanosedimentary rocks
Acid & intermediate volcanic rocks
Mafic volcanic rocks
Major fault
Minor fault
Thrust fault
Age (Volcanic)
Main City
Study Area
Volcanic rocks
Quaternary
Miocene- Pliocene
Eocene- Oligocene
Intrusive rocks
Eocene- Oligocene
Jurassic- Cretaceous
Ophiolite
Porphyry Cu (Au)
0 25 50 Km

Figure 1

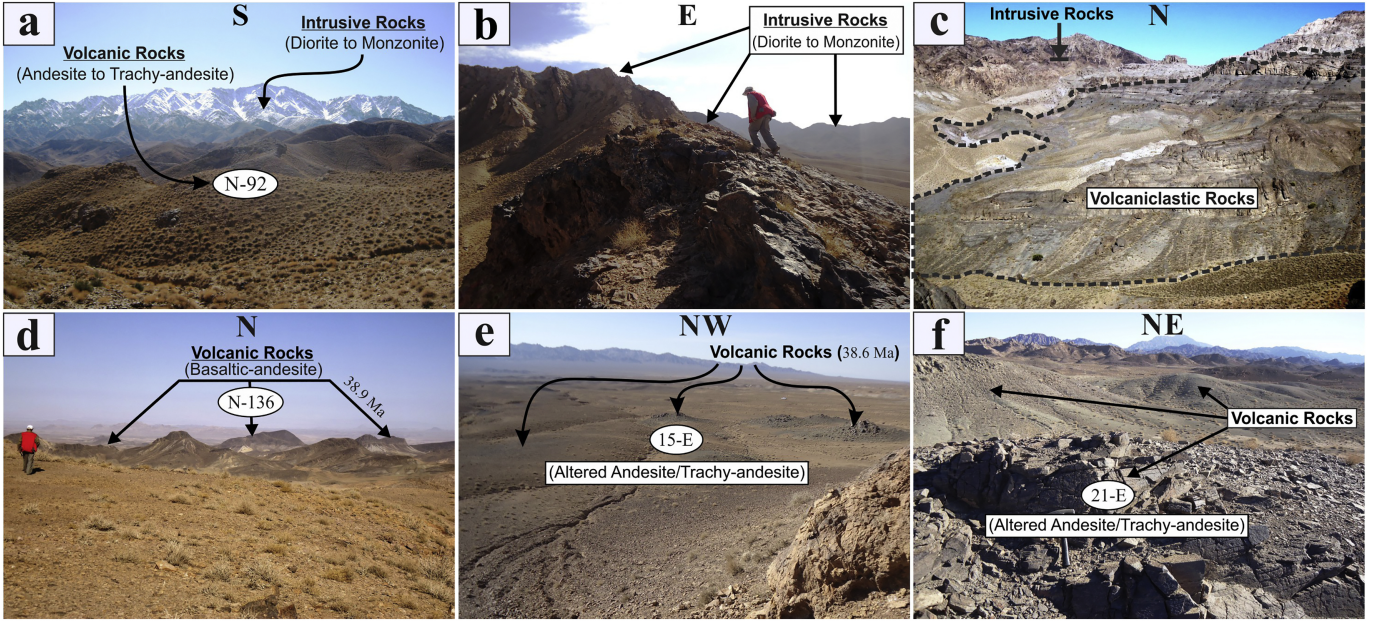
a
S
Intrusive Rocks
(Diorite to Monzonite)
Volcanic Rocks
(Andesite to Trachy-andesite)
N-92
b
E
Intrusive Rocks
(Diorite to Monzonite)
c
Intrusive Rocks
N
Volcaniclastic Rocks
d
N
Volcanic Rocks
(Basaltic-andesite)
N-136
38.9 Ma
e
NW
Volcanic Rocks (38.6 Ma)
15-E
(Altered Andesite/Trachy-andesite)
f
NE
Volcanic Rocks
21-E
(Altered Andesite/Trachy-andesite)

Figure 2

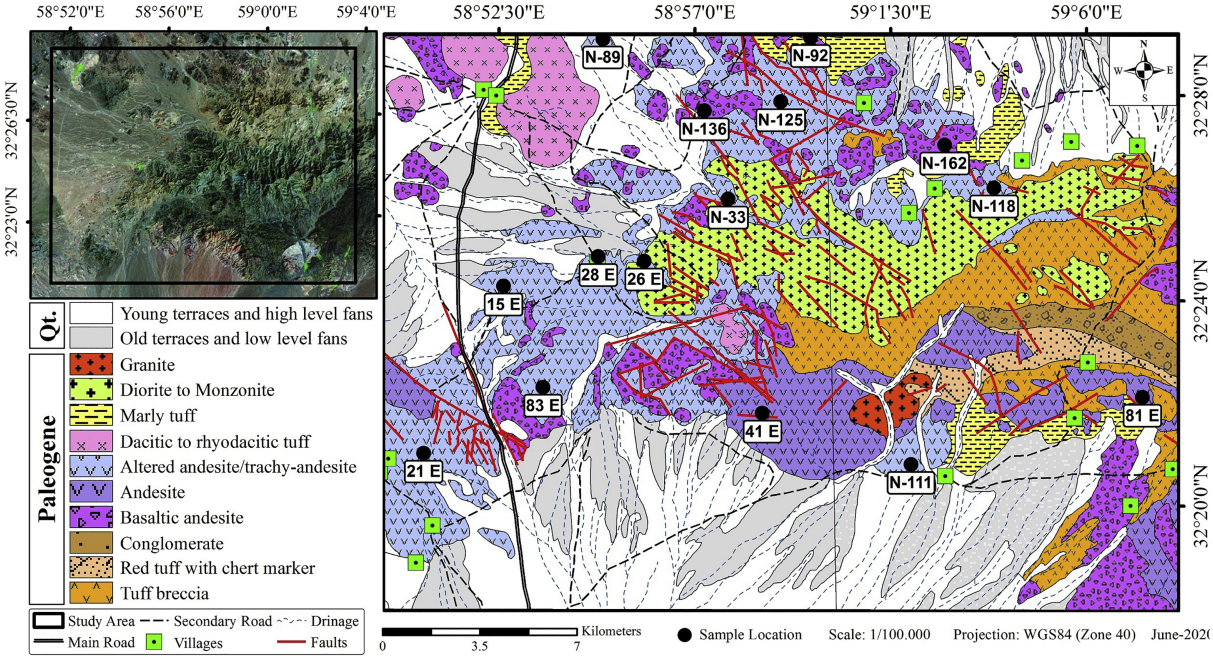
58°52'0"E
58°56'0"E
59°0'0"E
59°4'0"E
58°52'30"E
58°57'0"E
59°1'30"E
59°6'0"E
32°26'30"N
32°23'0"N
32°28'0"N
32°24'0"N
32°20'0"N
N-89
N-92
N-136
N-125
N-162
N-118
N-33
28 E
26 E
15 E
83 E
41 E
81 E
21 E
N-111
Qt.
Young terraces and high level fans
Old terraces and low level fans
Paleogene
Granite
Diorite to Monzonite
Marly tuff
Dacitic to rhyodacitic tuff
Altered andesite/trachy-andesite
Andesite
Basaltic andesite
Conglomerate
Red tuff with chert marker
Tuff breccia
Study Area
Secondary Road
Drinage
Main Road
Villages
Faults
Kilometers
0
3.5
7
Sample Location
Scale: 1/100.000
Projection: WGS84 (Zone 40)
June-202

Figure 3

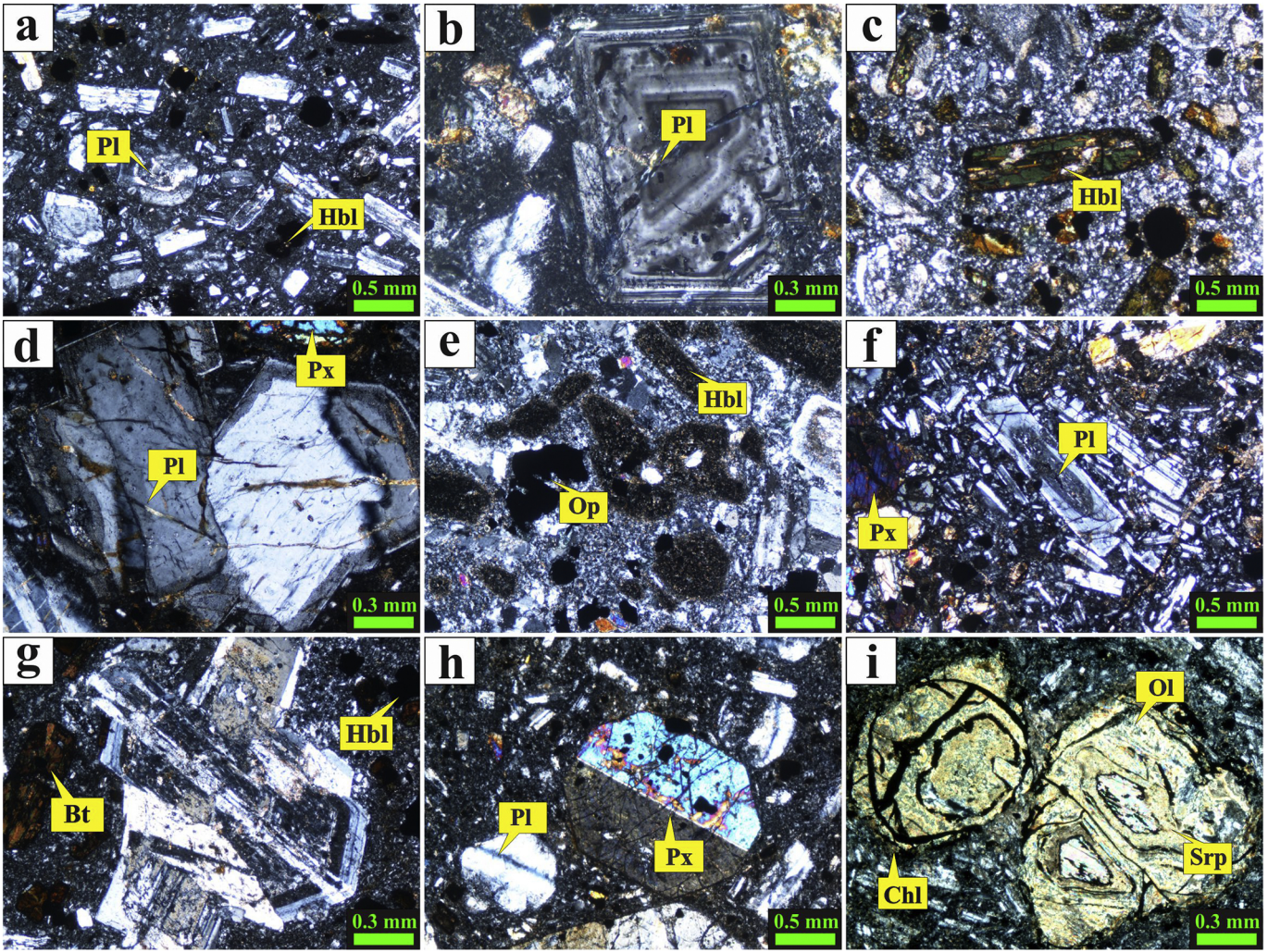
a
Pl
Hbl
0.5 mm
b
Pl
0.3 mm
c
Hbl
0.5 mm
d
Px
Pl
0.3 mm
e
Hbl
Op
0.5 mm
f
Pl
Px
0.5 mm
g
Hbl
Bt
0.3 mm
h
Pl
Px
0.5 mm
i
Ol
Srp
Chl
0.3 mm

Figure 4

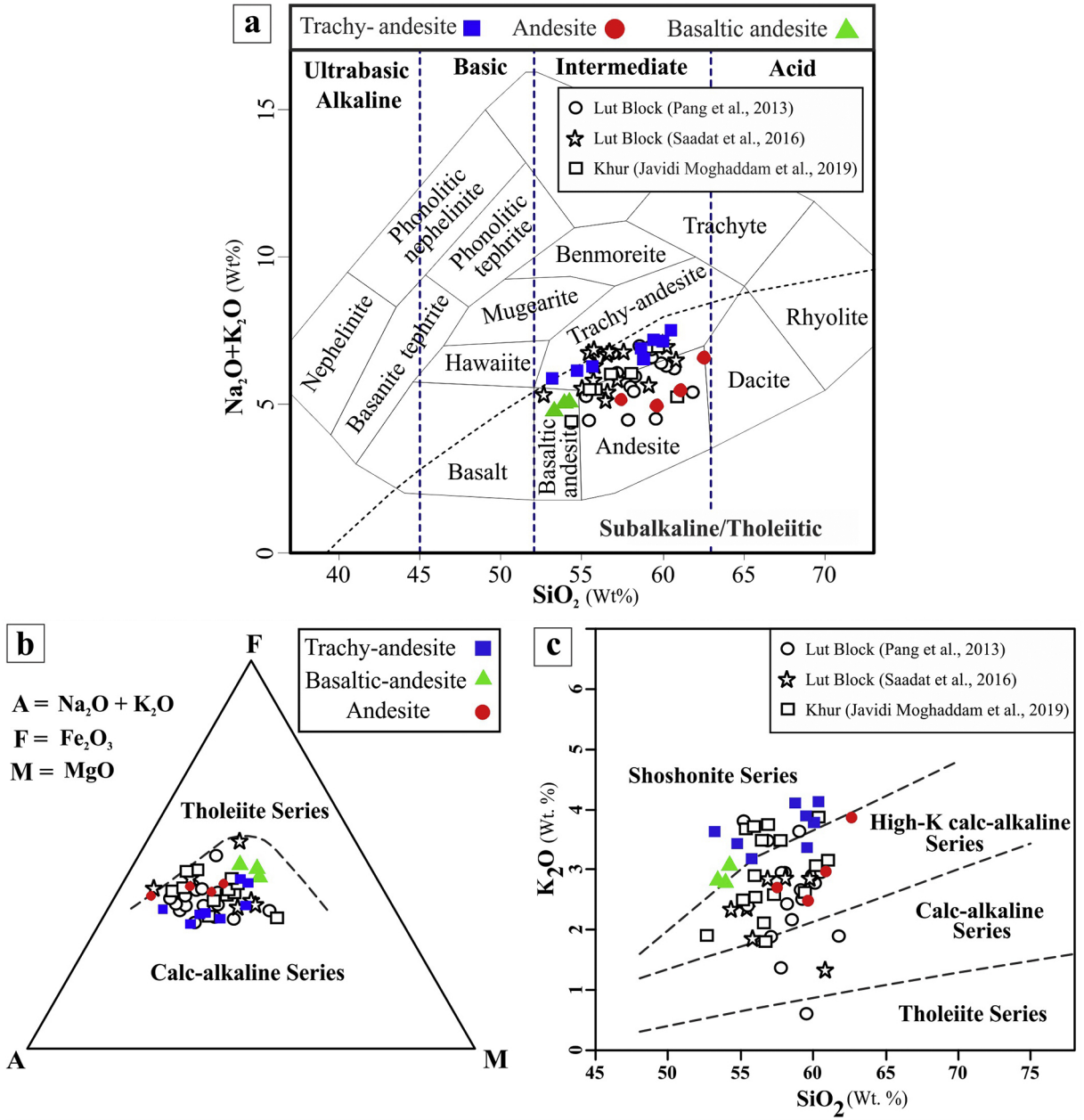
a
Trachy- andesite
Andesite
Basaltic andesite
Ultrabasic Alkaline
Basic
Intermediate
Acid
Lut Block (Pang et al., 2013)
Lut Block (Saadat et al., 2016)
Khur (Javidi Moghaddam et al., 2019)
Phonolitic nephelinite
Phonolitic tephrite
Trachyte
Benmoreite
Mugearite
Trachy-andesite
Rhyolite
Nephelinite
Basanite tephrite
Hawaiite
Dacite
Basaltic andesite
Andesite
Basalt
Subalkaline/Tholeiitic
Na2O+K2O (Wt%)
SiO2 (Wt%)
b
F
A = Na2O + K2O
F = Fe2O3
M = MgO
Trachy-andesite
Basaltic-andesite
Andesite
Tholeiite Series
Calc-alkaline Series
A
M
c
Lut Block (Pang et al., 2013)
Lut Block (Saadat et al., 2016)
Khur (Javidi Moghaddam et al., 2019)
Shoshonite Series
High-K calc-alkaline Series
Calc-alkaline Series
Tholeiite Series
K2O (Wt. %)
SiO2 (Wt. %)

Figure 5

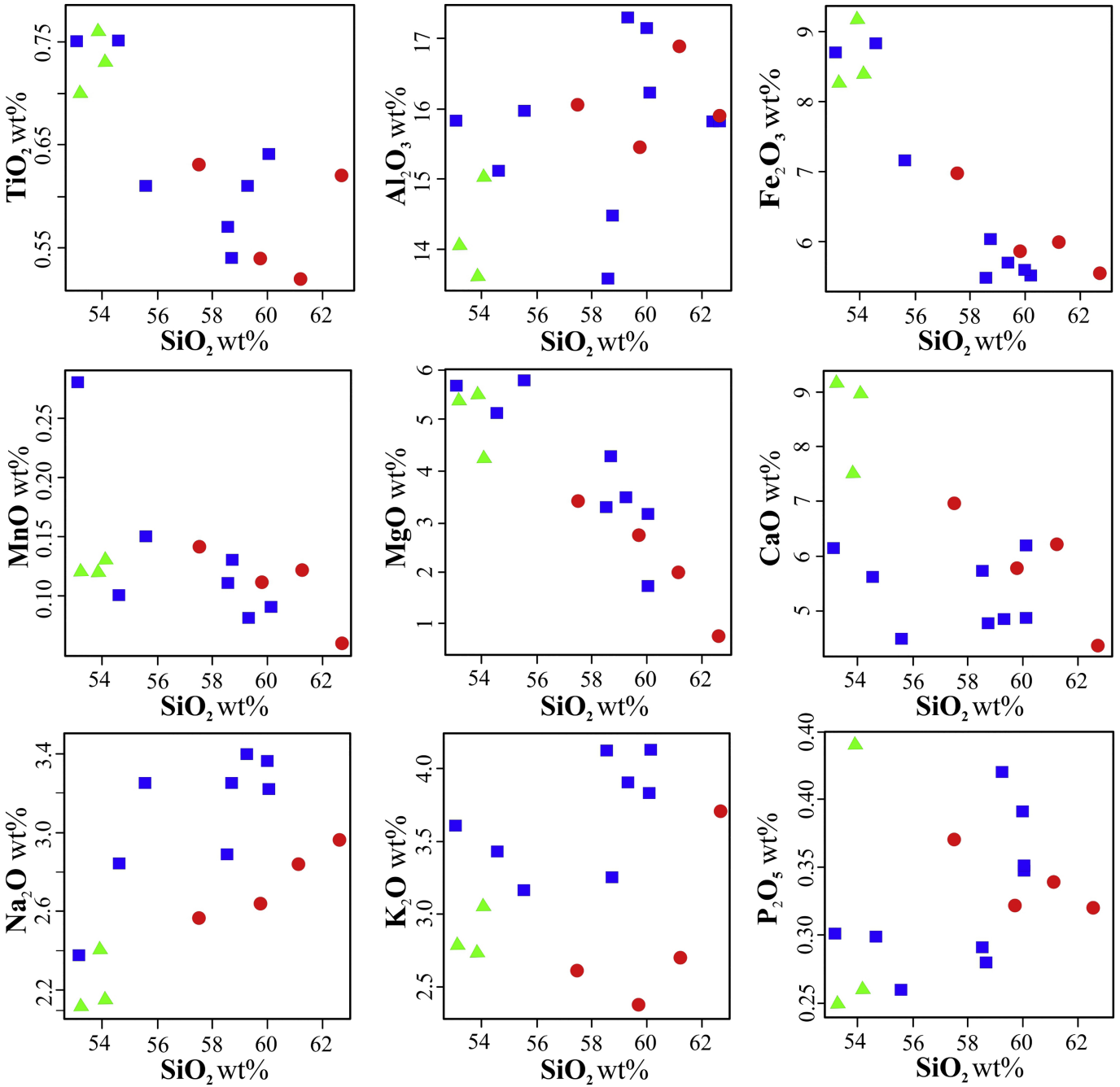
TiO2 wt%
0.55
0.65
0.75
Al2O3 wt%
14
15
16
17
Fe2O3 wt%
6
7
8
9
MnO wt%
0.10
0.15
0.20
0.25
MgO wt%
1
2
3
4
5
6
CaO wt%
5
6
7
8
9
Na2O wt%
2.2
2.6
3.0
3.4
K2O wt%
2.5
3.0
3.5
4.0
P2O5 wt%
0.25
0.30
0.35
0.40
54
56
58
60
62
SiO2 wt%

Figure 6

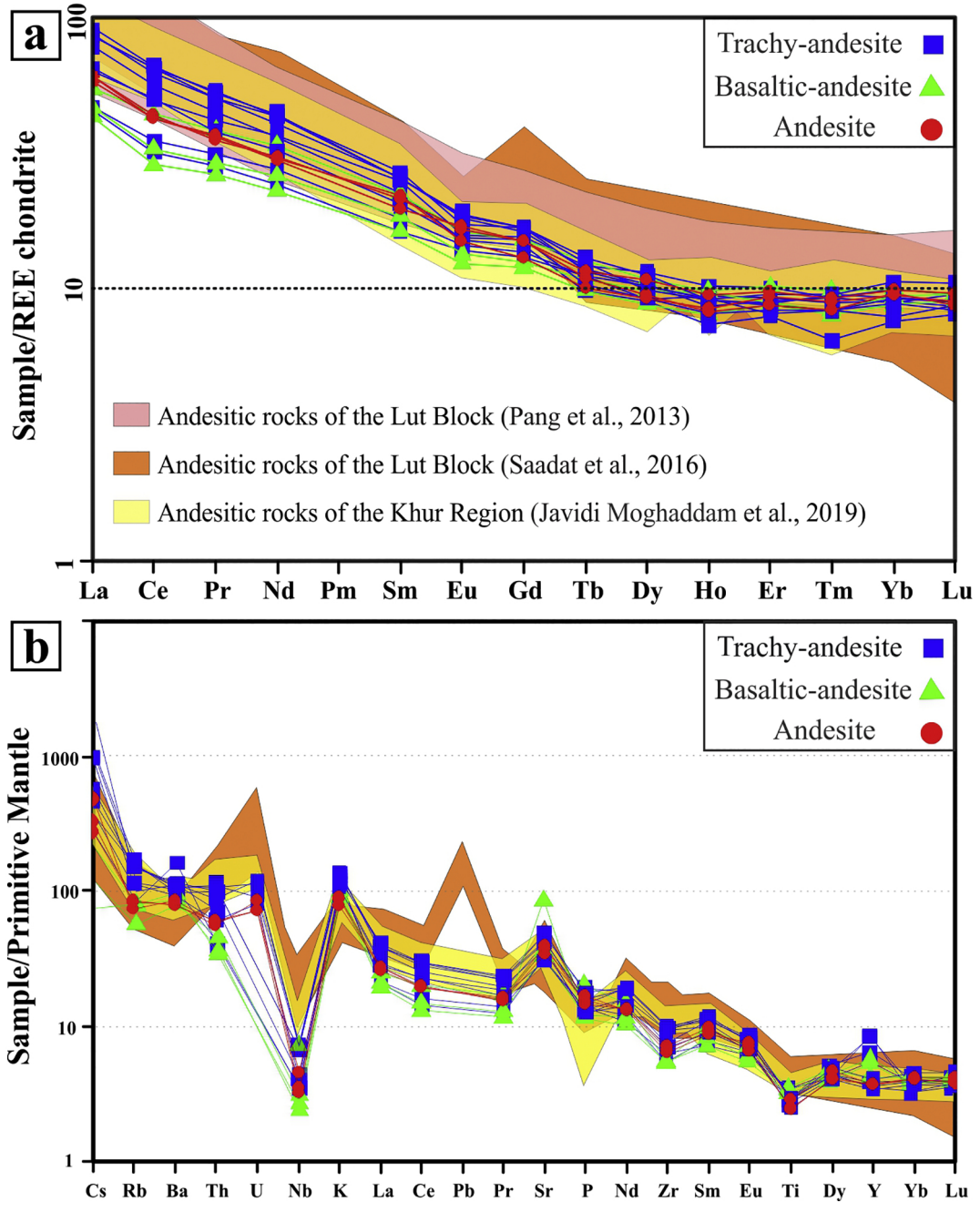
a
Trachy-andesite
Basaltic-andesite
Andesite
Sample/REE chondrite
100
10
1
Andesitic rocks of the Lut Block (Pang et al., 2013)
Andesitic rocks of the Lut Block (Saadat et al., 2016)
Andesitic rocks of the Khur Region (Javidi Moghaddam et al., 2019)
La Ce Pr Nd Pm Sm Eu Gd Tb Dy Ho Er Tm Yb Lu
b
Trachy-andesite
Basaltic-andesite
Andesite
Sample/Primitive Mantle
1000
100
10
1
Cs Rb Ba Th U Nb K La Ce Pb Pr Sr P Nd Zr Sm Eu Ti Dy Y Yb Lu

Figure 7

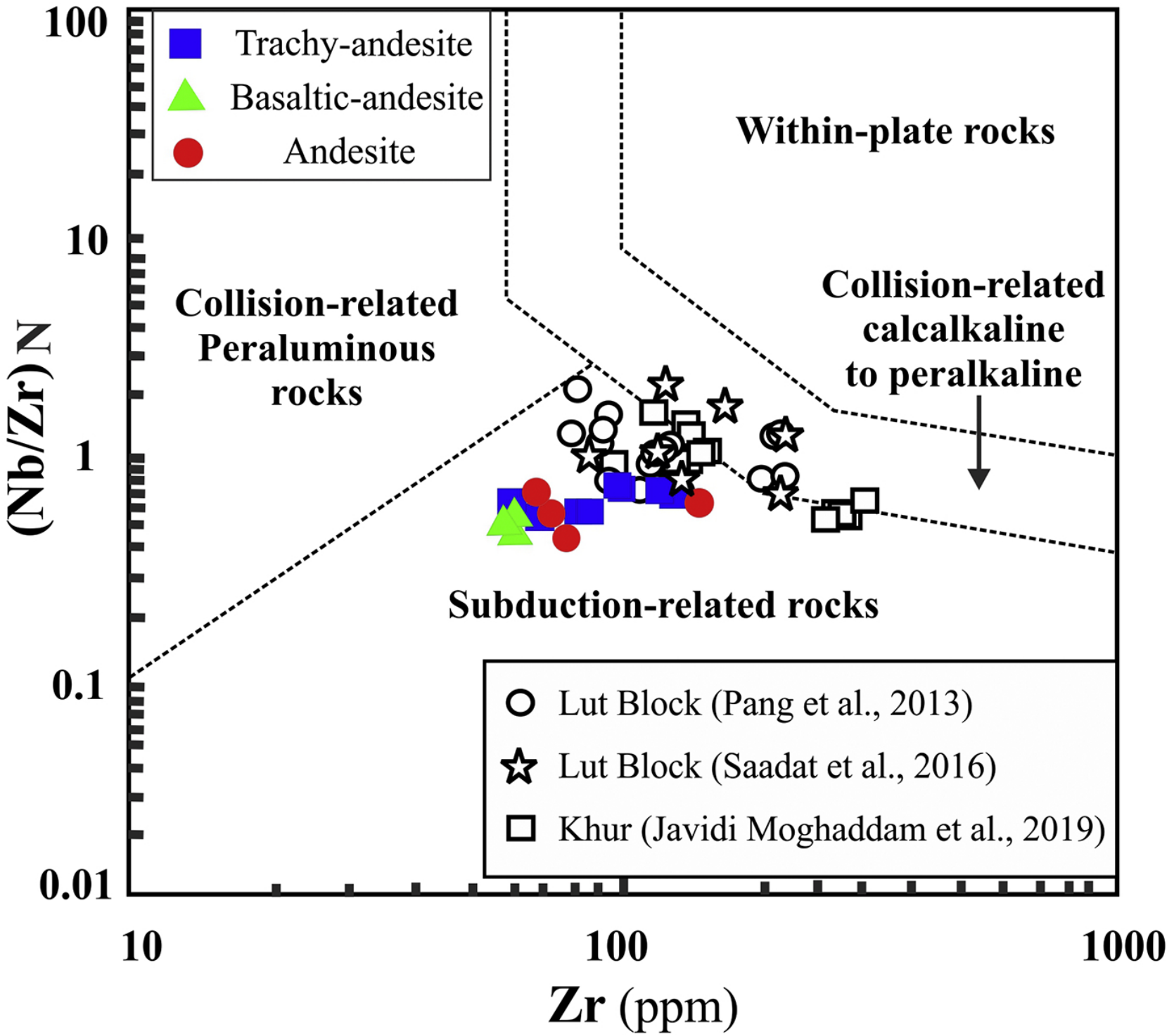
Trachy-andesite
Basaltic-andesite
Andesite
Within-plate rocks
Collision-related
Peraluminous
rocks
Collision-related
calcalkaline
to peralkaline
Subduction-related rocks
Lut Block (Pang et al., 2013)
Lut Block (Saadat et al., 2016)
Khur (Javidi Moghaddam et al., 2019)
100
10
1
0.1
0.01
(Nb/Zr) N
10
100
1000
Zr (ppm)

Figure 8

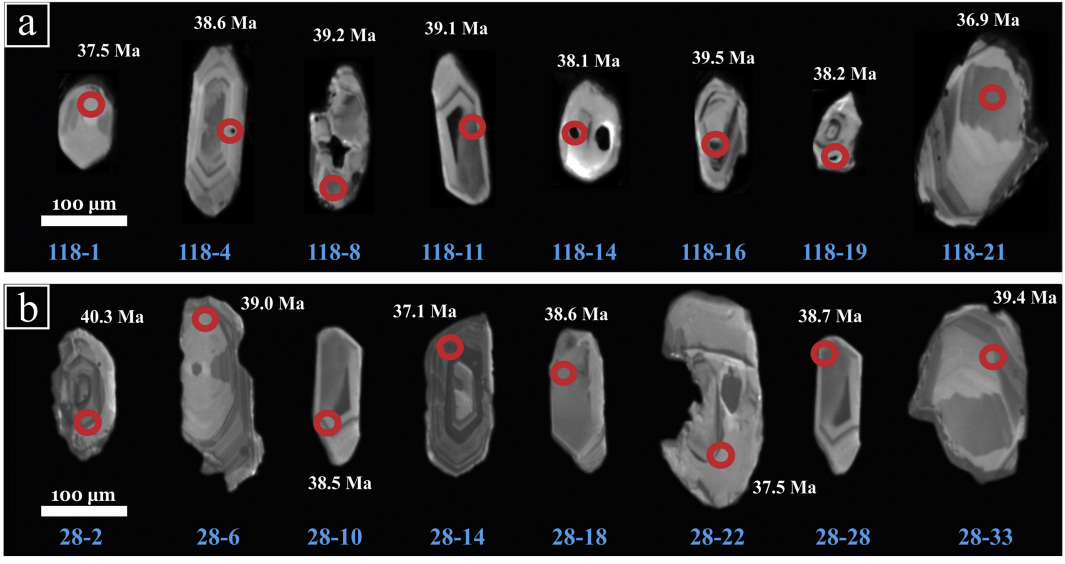
a
37.5 Ma
38.6 Ma
39.2 Ma
39.1 Ma
38.1 Ma
39.5 Ma
38.2 Ma
36.9 Ma
100 µm
118-1
118-4
118-8
118-11
118-14
118-16
118-19
118-21
b
40.3 Ma
39.0 Ma
37.1 Ma
38.6 Ma
38.7 Ma
39.4 Ma
38.5 Ma
37.5 Ma
100 µm
28-2
28-6
28-10
28-14
28-18
28-22
28-28
28-33

Figure 9

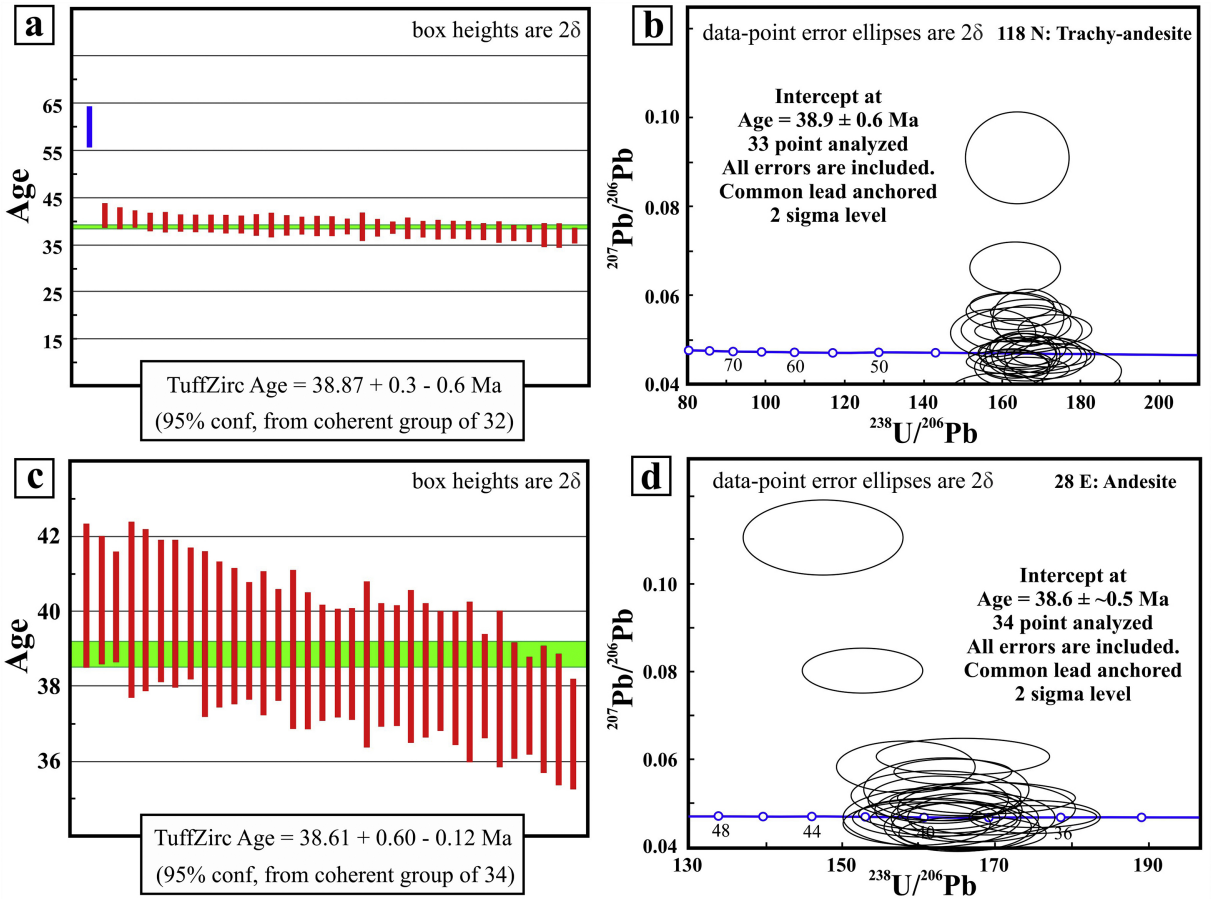
a
box heights are 2δ
Age
65
55
45
35
25
15
TuffZirc Age = 38.87 + 0.3 - 0.6 Ma
(95% conf, from coherent group of 32)
b
data-point error ellipses are 2δ
118 N: Trachy-andesite
Intercept at
Age = 38.9 ± 0.6 Ma
33 point analyzed
All errors are included.
Common lead anchored
2 sigma level
$^{207}Pb/^{206}Pb$
0.10
0.08
0.06
0.04
70
60
50
80
100
120
140
160
180
200
$^{238}U/^{206}Pb$
c
box heights are 2δ
Age
42
40
38
36
TuffZirc Age = 38.61 + 0.60 - 0.12 Ma
(95% conf, from coherent group of 34)
d
data-point error ellipses are 2δ
28 E: Andesite
Intercept at
Age = 38.6 ± ~0.5 Ma
34 point analyzed
All errors are included.
Common lead anchored
2 sigma level
$^{207}Pb/^{206}Pb$
0.10
0.08
0.06
0.04
48
44
40
36
130
150
170
190
$^{238}U/^{206}Pb$

Figure 10

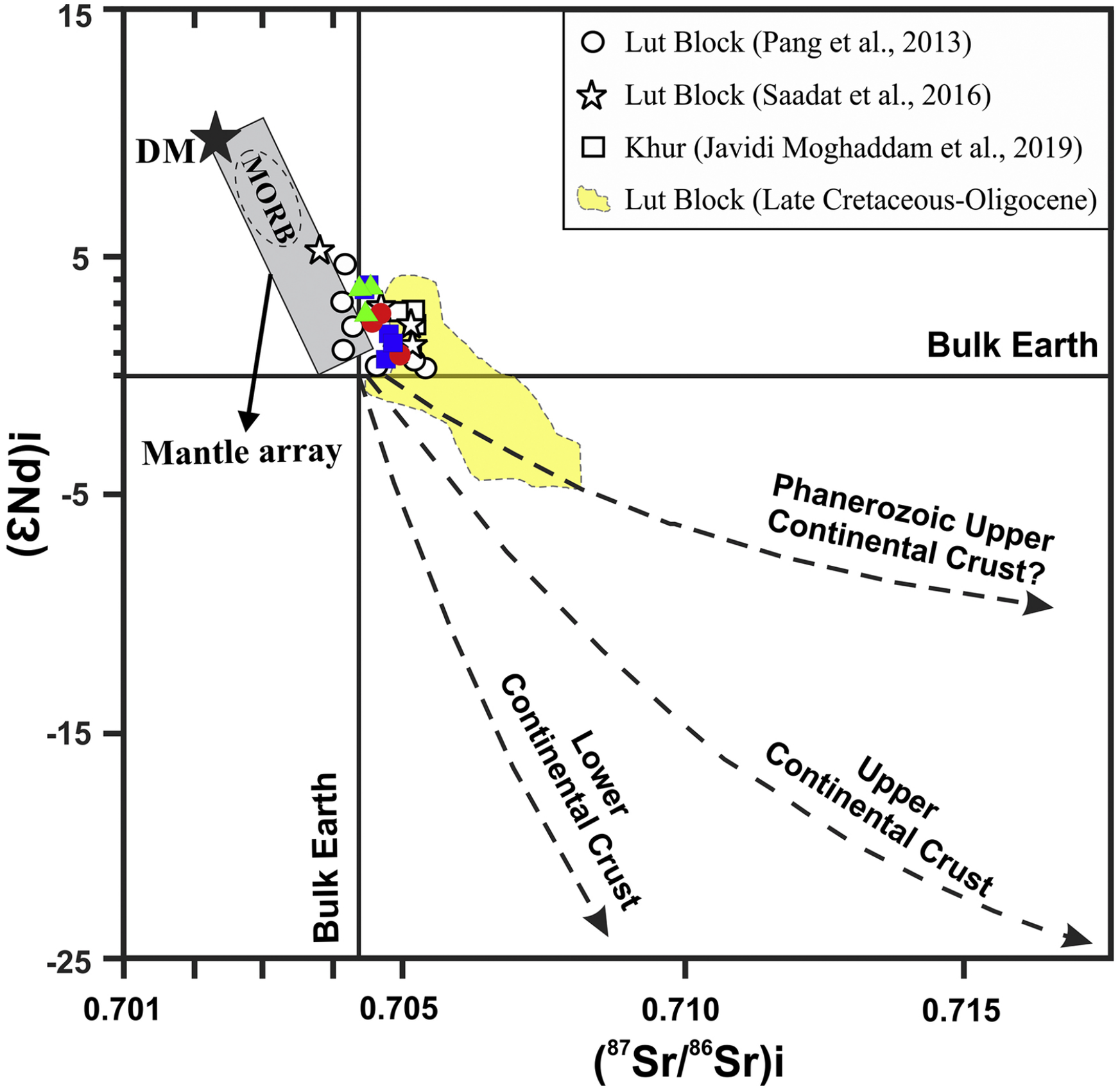
Lut Block (Pang et al., 2013)
Lut Block (Saadat et al., 2016)
Khur (Javidi Moghaddam et al., 2019)
Lut Block (Late Cretaceous-Oligocene)
DM
MORB
Mantle array
Bulk Earth
Phanerozoic Upper Continental Crust?
Upper Continental Crust
Lower Continental Crust
Bulk Earth
15
5
-5
-15
-25
0.701
0.705
0.710
0.715
(εNd)i
(87Sr/86Sr)i

Figure 11

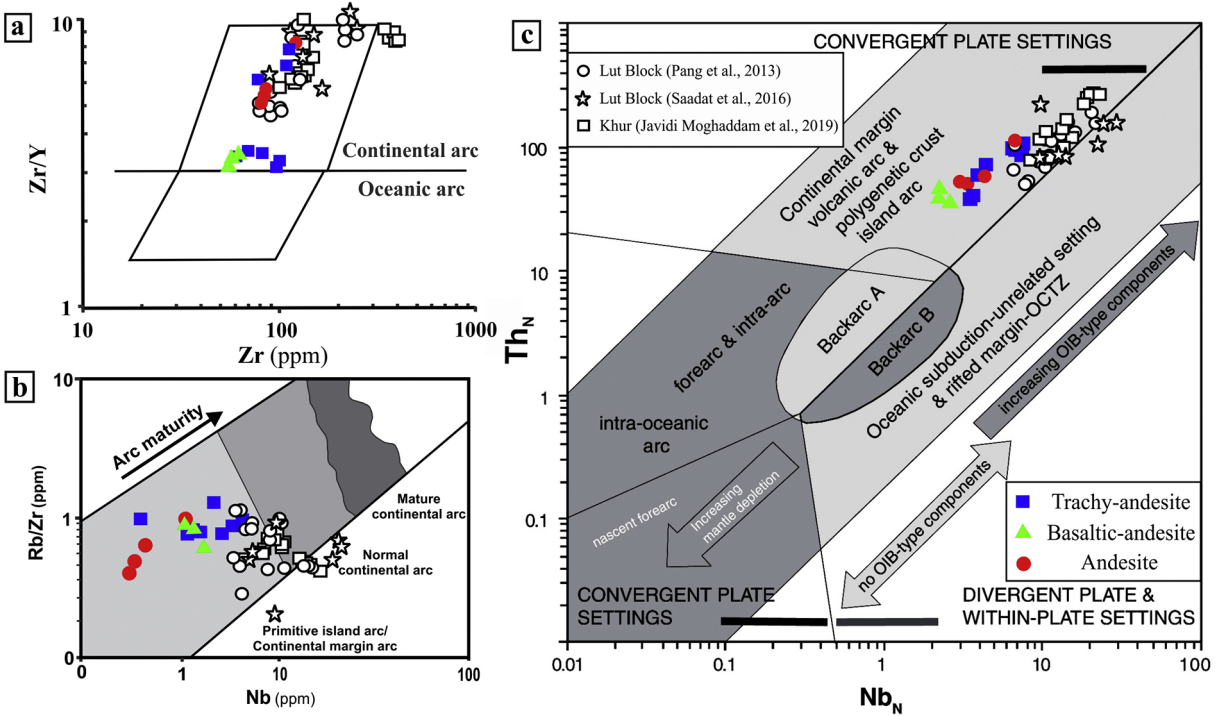
a
Zr/Y
Zr (ppm)
Continental arc
Oceanic arc
b
Rb/Zr (ppm)
Nb (ppm)
Arc maturity
Mature continental arc
Normal continental arc
Primitive island arc/ Continental margin arc
c
CONVERGENT PLATE SETTINGS
Lut Block (Pang et al., 2013)
Lut Block (Saadat et al., 2016)
Khur (Javidi Moghaddam et al., 2019)
Continental margin volcanic arc & polygenetic crust island arc
forearc & intra-arc
Backarc A
Backarc B
Oceanic subduction-unrelated setting & rifted margin-OCTZ
intra-oceanic arc
nascent forearc
Increasing mantle depletion
increasing OIB-type components
no OIB-type components
Trachy-andesite
Basaltic-andesite
Andesite
CONVERGENT PLATE SETTINGS
DIVERGENT PLATE & WITHIN-PLATE SETTINGS
Th_N
Nb_N

Figure 12

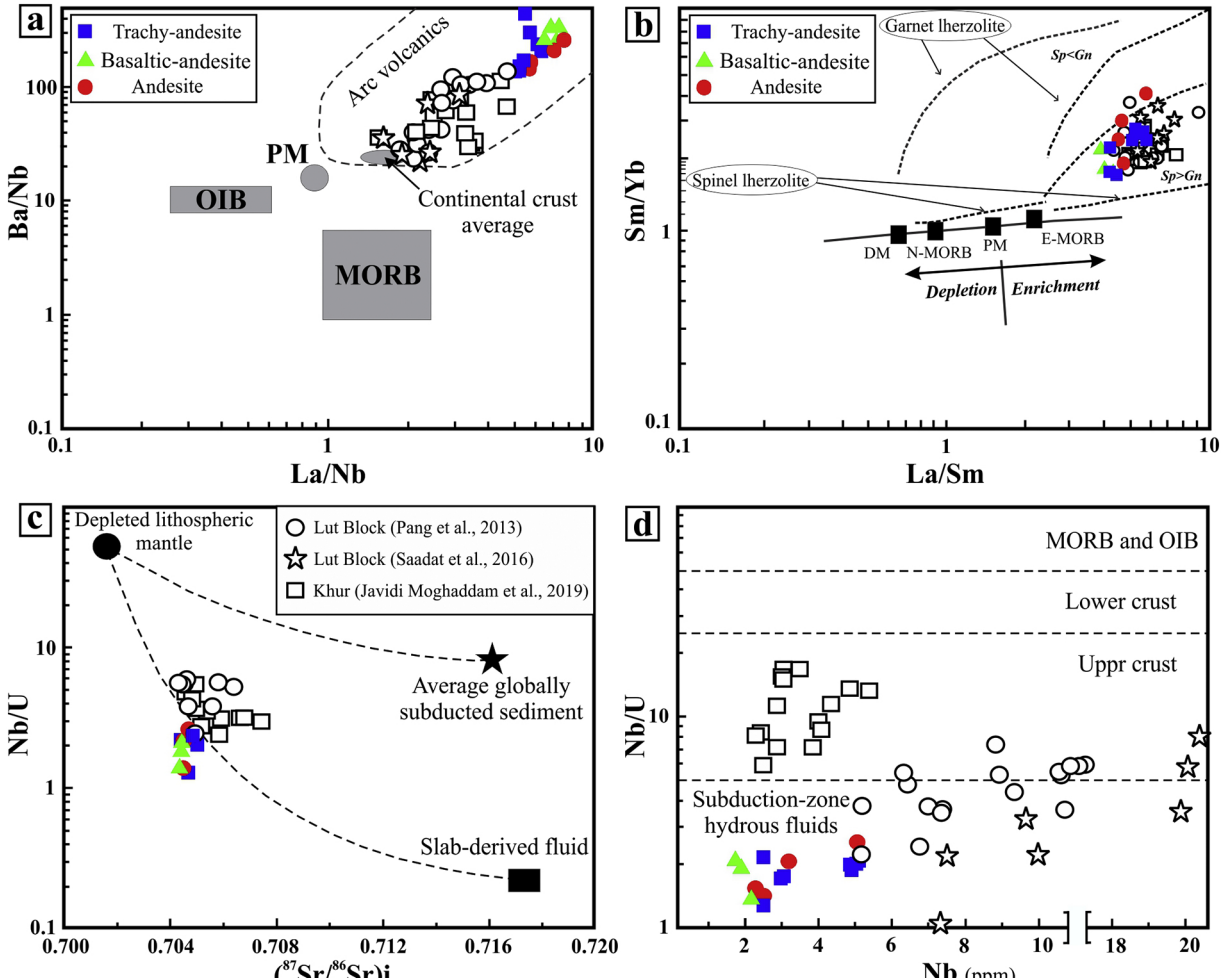
a
Trachy-andesite
Basaltic-andesite
Andesite
Arc volcanics
PM
OIB
MORB
Continental crust average
Ba/Nb
La/Nb
b
Trachy-andesite
Basaltic-andesite
Andesite
Garnet lherzolite
Sp<Gn
Sp>Gn
Spinel lherzolite
DM
N-MORB
PM
E-MORB
Depletion
Enrichment
Sm/Yb
La/Sm
c
Depleted lithospheric mantle
Lut Block (Pang et al., 2013)
Lut Block (Saadat et al., 2016)
Khur (Javidi Moghaddam et al., 2019)
Average globally subducted sediment
Slab-derived fluid
Nb/U
(87Sr/86Sr)i
d
MORB and OIB
Lower crust
Uppr crust
Subduction-zone hydrous fluids
Nb/U
Nb (ppm)

Figure 13

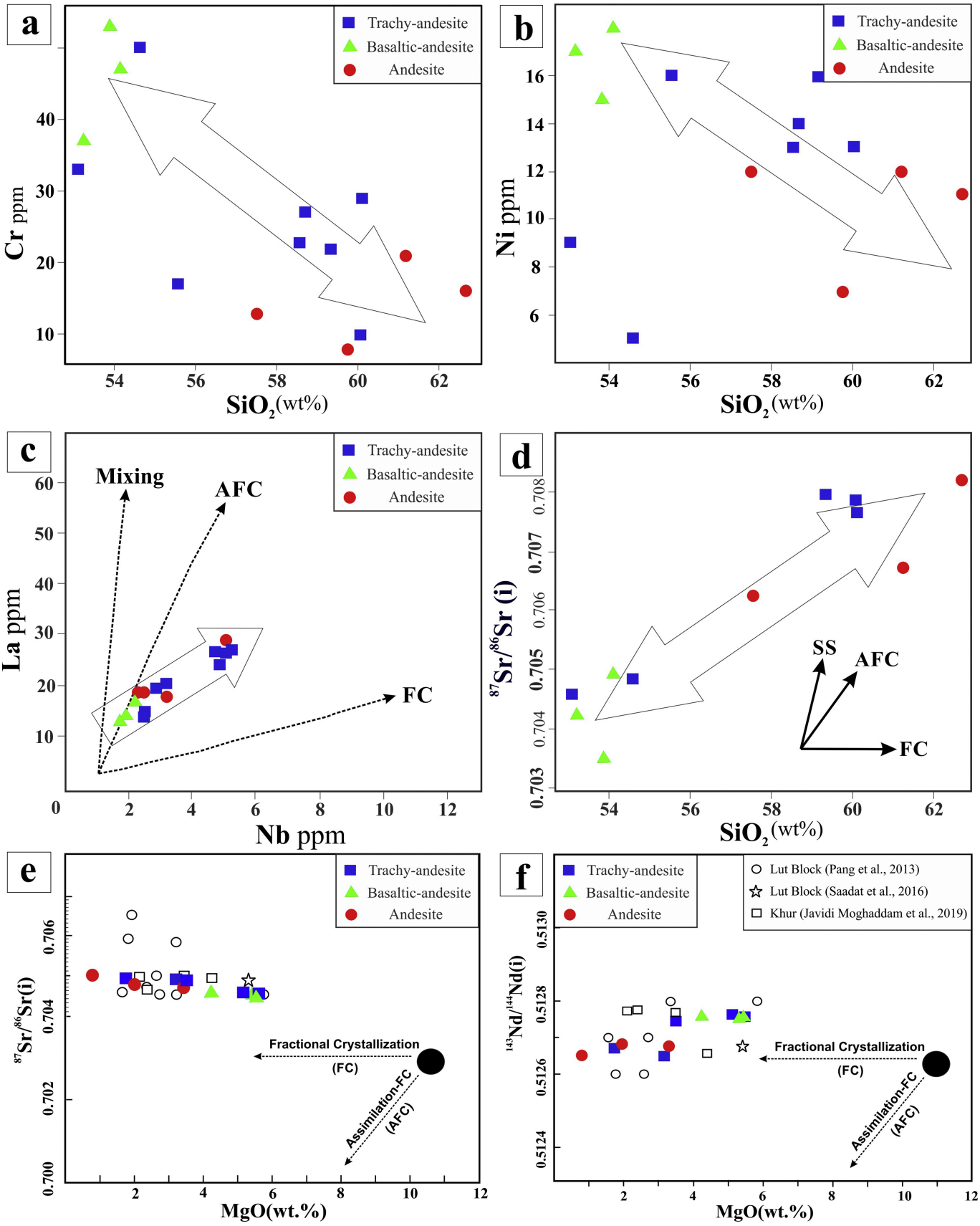
a
Trachy-andesite
Basaltic-andesite
Andesite
Cr ppm
SiO2(wt%)
b
Ni ppm
SiO2(wt%)
c
Mixing
AFC
FC
La ppm
Nb ppm
d
SS
AFC
FC
87Sr/86Sr (i)
SiO2(wt%)
e
Fractional Crystallization
(FC)
Assimilation-FC
(AFC)
87Sr/86Sr(i)
MgO(wt.%)
f
Lut Block (Pang et al., 2013)
Lut Block (Saadat et al., 2016)
Khur (Javidi Moghaddam et al., 2019)
143Nd/144Nd(i)
MgO(wt.%)

Figure 14

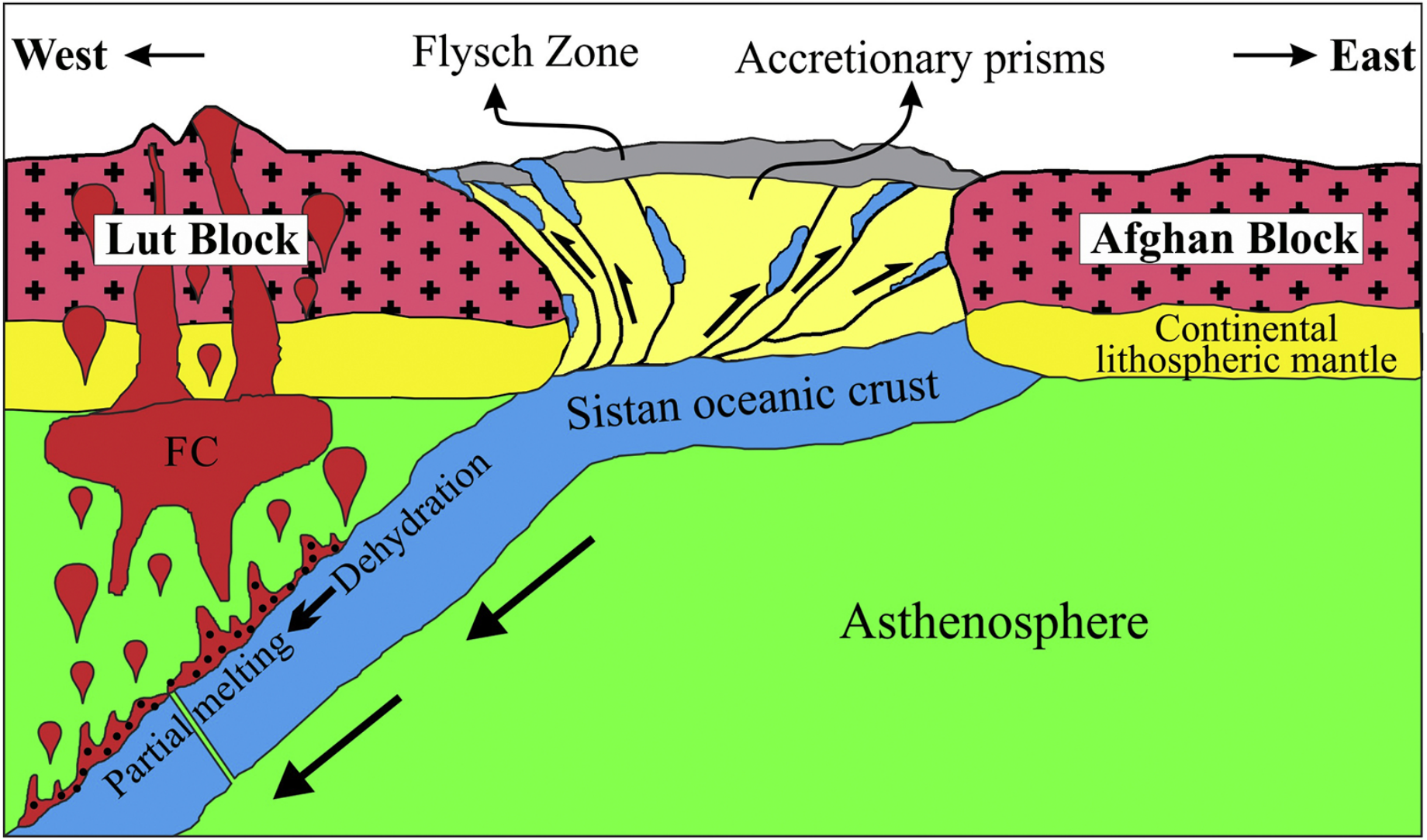
West
Flysch Zone
Accretionary prisms
East
Lut Block
Afghan Block
Continental
lithospheric mantle
Sistan oceanic crust
FC
Dehydration
Partial melting
Asthenosphere

Figure 15